

Microstructural material database for self-consistent clustering analysis of elastoplastic strain softening materials

Zeliang Liu^a, Mark Fleming^b, Wing Kam Liu^{b,*}

^a *Theoretical and Applied Mechanics, Northwestern University, Evanston, IL 60208, USA*

^b *Department of Mechanical Engineering, Northwestern University, Evanston, IL 60208, USA*

Received 31 August 2017; received in revised form 27 October 2017; accepted 3 November 2017

Available online 14 November 2017

Abstract

Multiscale modeling of heterogeneous material undergoing strain softening poses computational challenges for localization of the microstructure, material instability in the macrostructure, and the computational requirement for accurate and efficient concurrent calculation. In the paper, a stable micro-damage homogenization algorithm is presented which removes the material instability issues in the microstructure with representative volume elements (RVE) that are not sensitive to size when computing the homogenized stress–strain response.

The proposed concurrent simulation framework allows the computation of the macroscopic response to explicitly consider the behavior of the separate constituents (material phases), as well as the complex microstructural morphology. A non-local material length parameter is introduced in the macroscale model, which will control the width of the damage bands and prevent material instability.

The self-consistent clustering analysis (SCA) recently proposed by Liu et al. [1] provides an effective way of developing a microstructural database based on a clustering algorithm and the Lippmann–Schwinger integral equation, which enables an efficient and accurate prediction of nonlinear material response. The self-consistent clustering analysis is further generalized to consider complex loading paths through the projection of the effective stiffness tensor. In the concurrent simulation, the predicted macroscale strain localization is observed to be sensitive to the combination of microscale constituents, showing the unique capability of the SCA microstructural database for complex material simulations.

© 2017 Elsevier B.V. All rights reserved.

Keywords: Multi-scale damage models; Microstructural database; Data compression in model reduction; Self-consistent scheme; Concurrent simulation; Non-local damage model

1. Introduction

Multiscale simulation methods present significant advantages for computational mechanics due to their ability to analyze macroscopic structural performance while considering the effects of microscopic heterogeneities. While

* Corresponding author.

E-mail address: w-liu@northwestern.edu (W.K. Liu).

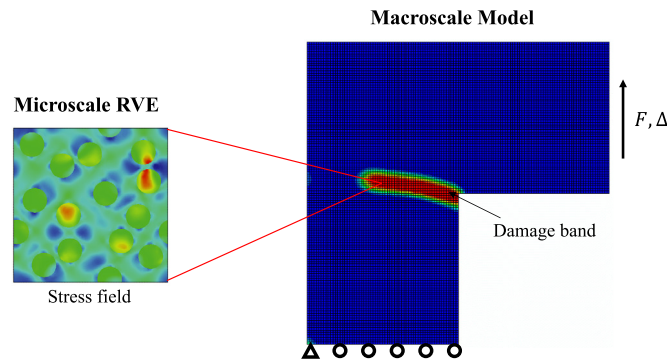


Fig. 1. Illustration of the RVE microstructural stress effects of inclusions in the material microstructure (left) during localization of a macroscale model (right).

great strides have been made, some core challenges still face multiscale methods, including accurate methods for homogenizing the microstructural representative volume element (RVE) undergoing strain localization, computation of strain localization with variable-sized microstructural features, and the ability to conduct efficient concurrent simulations.

1.1. Core challenge 1: homogenization with localization

The presence of voids and inclusions in a material will result in a non-uniform stress and strain field at the microstructural scale (see Fig. 1). Continued straining will result in nucleation and coalescence of microstructural voids in a ductile material, leading to shear banding, localization, and fracture [2]. The resolution required to numerically predict the onset and development of these phenomena exceeds the available computational resources. The concurrent multiscale methods of McVeigh, Vernerey, and Liu [3] have shown promise for addressing this class of problems through the use of representative volume elements (RVEs) to compute material behavior at the microstructure. The microstructure RVE can be coupled with macroscopic finite element models to predict overall structural behavior which accounts for the microstructural character.

Strain softening due to localization poses computational challenges at the microscopic levels for concurrent multiscale methods. Direct application of a material damage model in the microstructure results in non-physical results due to material instability. To date, multiscale modeling coupled with material damage is still not well explored [4]. Most multiscale methods require an additional microscale material length parameter to regularize the ill-posed boundary value problem in the microscale RVE. However, the relationship between the macroscale and microscale length parameters is usually not physically justified, and it is arguable that the microscale RVE model actually does not provide any information on how to determine the macroscale material length parameter. Instead, it merely moves the continuum localization problem one scale down [5]. Even if the microscale RVE model is regularized by a length parameter without justifying its physical basis, the homogenization problem with the localization effect is still not well defined. In the strain-softening region, the overall homogenized stress–strain response strongly depends on the size of the RVE, which is actually contradictory to the definition of an RVE. Unfortunately, this issue is very often not acknowledged in the literature for multiscale homogenization with strain-softening and localization effects.

In Section 2, a novel micro-damage algorithm is proposed that alleviates the material instability at the microstructural level. The homogenized behavior in the strain softening region is not sensitive to the RVE size.

1.2. Core challenge 2: macroscopic non-local damage model for strain localization

Material damage models [6] can be used to model material localization and failure while accounting for the heterogeneous effects of microscale inclusions (see Fig. 1). However, modeling material damage and localization with continuum damage methods poses stability challenges because the damaged region of the material will always localize to a single layer of elements. Further mesh refinement results in thinner localization bands and reduced

energy dissipation due to the material damage, which is contrary to the physical energy dissipation of localization. This challenge occurs due to the local material strain-softening effect, in which the tangential stiffness matrix is no longer positive definite, leading to an imaginary wave speed. As such, the boundary value problem becomes ill-posed, and the continuum form of the equilibrium condition becomes unstable. Thus, the numerical solution loses objectivity with respect to the mesh choice and exhibits spurious mesh sensitivity. Several methods have been proposed to resolve this mesh-dependence problem due to the strain-softening effect, such as non-local damage model [7], micromorphic continuum [2,3,8–10], phase-field fracture [11,12], crack band theory [13] and eigen-erosion method [14]. Among all these methods, a material length parameter or the material fracture energy, G_f (energy per unit area), are introduced to regularize the original ill-posed boundary value problem. For example, in phase-field model for quasi-brittle fracture [11], G_f is defined as a material constant measured from experiment, which limits the energy dissipation per unit area in the crack. Meanwhile, the material length parameter helps to diffuse the fracture singularity over a finite damaged region, making it numerically solvable. In non-local damage models [7], the material length parameter is introduced to spread the damaged region over a finite domain, which allows the objectivity of the numerical solution to be recovered. This material length parameter is either empirically-derived based on microstructural information (e.g. material characteristic length), or experimentally calibrated using fracture energy or size-effect testing results.

In Section 3, a non-local macroscopic damage model is introduced which couples the homogenized stress from the microstructural RVE with a macroscopic characteristic length and a weighting function. This method alleviates the material instability in the macroscopic model due to material damage.

1.3. Core challenge 3: efficient concurrent simulations

Accurate and efficient computational methods for predicting fracture and damage of engineering materials are essential to design and failure analysis of materials with non-uniform or heterogeneous microstructural properties. Successful material models need to capture the non-trivial inter-dependence between material constituents at small scales that lead to dramatic performance effects in the macro-scale response. Mechanistic understanding of this structure–property relation across material length scales will also enable the development of material microstructural database, which will accelerate material design and manufacturing [15,16]. This structure–property feedback loop enables the design of new material systems with new capabilities. In mathematical physics, structure is interpreted as the non-local interaction of the microstructural clusters, and property is interpreted as the virtual work at the corresponding material point. Computational design of experiments and data mining techniques offer the ability to discover the influence of the microstructure on the macroscopic material behavior.

Linking the microstructural character to the macroscopic inelastic behavior is an ongoing challenge and the subject of continued research. One area of particular interest is material fracture and failure analysis. This is typically accomplished by using fracture mechanics or continuum damage mechanics, which are macroscopic methods that are not sensitive to the material microstructure and require extensive testing and model calibration for new materials [6,17–20]. Concurrent multiscale methods [21–28] attempt to avoid the closed-form constitutive laws and the calibration process by directly establishing the connection between the microstructure and the macro-response of materials. These methods link every macroscale integration or material point to a representative microscopic material domain, which is solved by the microscale equilibrium condition. Following homogenization, the microscale model can provide the macroscale stress–strain responses during the analysis. The integration of microstructure reconstruction and high-fidelity multiscale predictions of the materials behavior leads to the generation of vast amounts of reliable data [29].

A drawback of multiscale methods is the computational expense required to accurately assess the stress–strain behavior of the microstructural RVE. On one hand, analytical approaches, such as rules of mixtures and theoretical micromechanics methods [30–34], are efficient, but lose accuracy for irregular morphologies and nonlinear history-dependent properties. In contrast, direct numerical simulations (DNS), such as finite element method (FEM) [21,35] and fast Fourier transform (FFT)-based method [36], offer high accuracy at the expense of prohibitive computational costs. Because of this, they are not applicable to concurrent simulations and material design. Data-driven reduced order modeling has been introduced for predicting the effective mechanical properties in a manner that balances computational cost and accuracy. These methods extract patterns of material behavior from a priori simulations, which expedite the calculations in the prediction stage. For heterogeneous hyperelastic materials, various data-driven approaches have been proposed to construct the overall energy surface of the RVE [29,37–39]. For history-dependent plastic material, the model reduction procedure can be more complex. Two examples are non-uniform

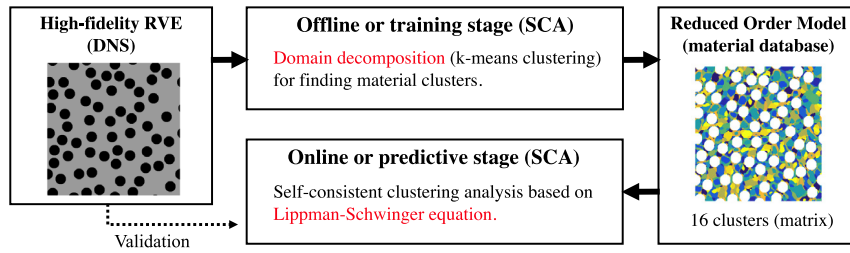


Fig. 2. Flowchart summarizing the self-consistent clustering analysis (SCA) for model reduction. Clusters in the inclusion phase are not shown.

transformation field analysis (NTFA) [40–42] and variants of the principle component analysis [43–45] or proper orthogonal decomposition (POD) [46–48]. In [42], Michel and Suquet enhanced the NTFA with the reduced evolution equations (or coarse dynamics), and applied it to the homogenization of elasto-viscoplastic materials. Oliver et al. [48] used POD to find a low-dimensional space of the displacement fluctuations and fitted the reduced order model into a concurrent multiscale fracture problem [48]. However, both NTFA and POD methods require extensive *a priori* simulations for interpolating nonlinear inelastic material behaviors, and the offline stages need to be recomputed for different combinations of material constituents.

Recently, the self-consistent clustering analysis (SCA) of Liu et al. [1] has been shown to greatly reduce computational expense through the use of novel data mining techniques based on clustering. This method uses RVE clustering techniques (see Fig. 2) to create a microstructural database from the high-fidelity simulation data in an offline training stage and homogenizes the reduced system based on a self-consistent scheme in the online predicting stage. With only linear elastic simulations in the offline stage, SCA has demonstrated a powerful trade-off between accuracy and efficiency in predicting elasto-plastic behavior with no strain softening [1]. SCA has also been shown to accelerate material behavior predictions (e.g. toughness) within a computational data-driven framework of material design under uncertainty [29].

1.4. Outline of the paper

The paper first introduces a new micro-damage homogenization algorithm in Section 2 and a non-local macroscopic damage model in Section 3. Section 4 presents the Lippmann–Schwinger equation for the self-consistent clustering analysis (SCA) online stage with a new self-consistent scheme based on projection of the effective stiffness tensor. This ensures the convergence of the self-consistent scheme under complex loading paths within a concurrent simulation. In Section 5, the microscale material laws are defined and the homogenized stress–strain response of the RVE is investigated. The accuracy and efficiency of the proposed method are validated against direct numerical simulation (DNS). In Section 6, concurrent simulations of a multiscale localization problem are performed, enabled by the SCA method. With the same SCA microstructural database, different macroscale localization patterns can be observed for different combinations of microscale constituents.

2. Multiscale damage model with a micro-damage algorithm

2.1. Mechanics

Material fracture is sensitive to the microstructure and evaluating these effects requires a multiscale modeling approach which incorporates these details. A material’s microstructure can consist of voids or inclusions which will lead to a non-uniform stress and strain state in the microstructure. Multiscale modeling couples the microstructural stress state with the macroscopic calculation to capture the effects of the microstructure in a macroscopic calculation.

The virtual internal work density at a macroscopic material point can be written as

$$\delta W^{\text{int}} = \boldsymbol{\sigma}_M : \delta \boldsymbol{\varepsilon}_M = \frac{1}{|\Omega|} \int_{\Omega} \boldsymbol{\sigma}_m : \delta \boldsymbol{\varepsilon}_m d\Omega, \quad (1)$$

where $|\Omega|$ is the volume of the microstructural RVE, and σ_m and $\delta\epsilon_m$ are the microstructural stress and virtual strain, respectively. The macroscopic stress σ_M and macroscopic virtual strain $\delta\epsilon_M$ can be computed using the Hill–Mandel Lemma to integrate these quantities over the microstructural RVE as

$$\sigma_M = \frac{1}{|\Omega|} \int_{\Omega} \sigma_m d\Omega \quad \text{and} \quad \delta\epsilon_M = \frac{1}{|\Omega|} \int_{\Omega} \delta\epsilon_m d\Omega. \quad (2)$$

In this paper, the subscript m represents the microscopic quantities, and the subscript M represents the macroscopic homogenized quantities.

For an elasto-plastic material, the constitutive law in the microstructure can be written as

$$\sigma_m = \mathbf{C}_m : \epsilon_m^{el} = \mathbf{C}_m : (\epsilon_m - \epsilon_m^{pl}) \quad (3)$$

where \mathbf{C}_m is the microscopic elastic stiffness tensor, and ϵ_m^{el} and ϵ_m^{pl} are the microscopic elastic strain and plastic strain, respectively. The total strain ϵ_m at a point within the microstructure is given by

$$\epsilon_m = \int d\epsilon_m \quad (4)$$

where $d\epsilon_m$ is the microstructural strain increment due to an associated macroscopic strain increment $d\epsilon_M$, applied as boundary conditions on the microstructural RVE. According to the Hill–Mandel lemma, the homogenized stress σ_M can be computed by averaging the microstructural stress σ_m in the RVE. Through this homogenization process, the mechanical response at each macro material/integration point is coupled with a microscale RVE model. Meanwhile, the computed microscopic history-dependent internal variables are stored in the RVE for continued analysis. This concurrent framework is advantageous since the constitutive law can be adjusted on the fly based on the microstructural characteristics. The multiscale framework obviates the need for a cumbersome equation-based phenomenological constitutive law to account for the behavior of history-dependent material with complex micro-morphologies and nonlinear behavior, such as plasticity.

2.2. Strain softening and damage

The homogenization scheme introduced in Section 2.1 may encounter stability problems when the material experiences strain-softening, such as material failure described by a progressive damage model. For an elasto-plastic material with damage, the damaged microstructural stress can be written as

$$\sigma_m^d = (1 - d_m) \mathbf{C}_m : \epsilon_m^{el} = (1 - d_m) \mathbf{C}_m : (\epsilon_m - \epsilon_m^{pl}), \quad (5)$$

where d_m is a non-decreasing scalar damage parameter describing the irreversible isotropic damage process. Anisotropic damage can also be considered, but the scalar damage parameter needs to be replaced by a tensor. This damage parameter acts on the stress of a reference elasto-plastic material,

$$\sigma_m^0 = \mathbf{C}_m : \epsilon_m^{el} = \mathbf{C}_m : (\epsilon_m - \epsilon_m^{pl}), \quad (6)$$

which gives

$$\sigma_m^d = (1 - d_m) \sigma_m^0. \quad (7)$$

This reference elasto-plastic material stores the history-dependent state variables and provides the relationship between the elastic strain ϵ_m^{el} and plastic strain ϵ_m^{pl} . The damage parameter can be written as a function of state variables \mathbf{q}_m (e.g. the effective plastic strain),

$$d_m = d_m(\mathbf{q}_m). \quad (8)$$

The progressive damage model directly applied to the microstructural RVE suffers from material instability due to non-physical strain softening, leading to results in which the localization occurs in very narrow bands of elements. Since no regularization is introduced in this example, the width of the band depends on the mesh size. Even if the microscale RVE is regularized with a physical band width, the homogenized macroscopic stress–strain response still strongly depends on the RVE size, so that it cannot represent the material behavior at local macroscopic material point.

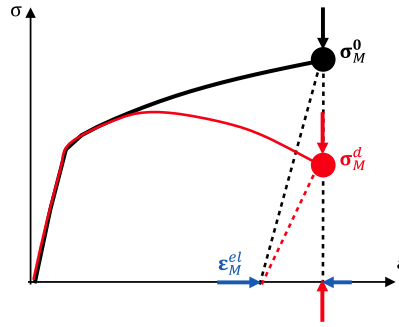


Fig. 3. Illustration of the micro-damage algorithm on the macroscopic stress–strain curve.

2.3. Stabilized micro-damage algorithm

A micro-damage stabilization algorithm is proposed which removes the material strain softening instability associated with traditional damage models. This is accomplished by introducing a reference elasto-plastic RVE and decoupling the damage from the plastic evolution. The effective macroscopic material law with damage is written as

$$\sigma_M^d = \mathbf{C}_M^d : \epsilon_M^{\text{el}} = \mathbf{C}_M^d : (\epsilon_M - \epsilon_M^{\text{pl}}), \quad (9)$$

where σ_M^d is the macroscopic stress of the damaged RVE, and \mathbf{C}_M^d is the macroscopic effective elastic stiffness tensor of the damaged RVE. Moreover, ϵ_M^{el} and ϵ_M^{pl} are the macroscopic effective elastic strain and plastic strain, respectively. The effective material law of the reference elasto-plastic RVE can be written as

$$\sigma_M^0 = \mathbf{C}_M : \epsilon_M^{\text{el}} = \mathbf{C}_M : (\epsilon_M - \epsilon_M^{\text{pl}}), \quad (10)$$

where σ_M^0 is the macroscopic stress of the undamaged reference RVE, whose effective elastic stiffness tensor is denoted by \mathbf{C}_M . Assuming the damaged elasto-plastic RVE has the same macroscopic effective elastic strain (or effective plastic strain), the following relationship between σ_M^d and σ_M^0 exists

$$\sigma_M^d = \mathbf{C}_M^d : [(\mathbf{C}_M)^{-1} : \sigma_M^0]. \quad (11)$$

In a general multi-dimensional heterogeneous material, the macroscopic effective plastic strain ϵ_M^{pl} is not necessarily a volume average of the microscopic plastic strain ϵ_m^{pl} . According to the definition of the macroscopic material law in Eq. (10), σ_M^0 should vanish if ϵ_M coincides with ϵ_M^{pl}

$$\sigma_M^0 = \mathbf{0}, \quad \text{if } \epsilon_M = \epsilon_M^{\text{pl}} \quad (\text{or } \epsilon_M^{\text{el}} = \mathbf{0}). \quad (12)$$

The stabilized micro-damage algorithm computes the effective macroscopic quantities in Eqs. (9) and (10), as illustrated in Fig. 3.

A strain increment at a macroscopic material point is passed to the reference elasto-plastic RVE as a homogenized strain increment, $d\epsilon_M$, and applied as a boundary condition. The microscopic material law in the RVE is

$$\sigma_{m1} = \mathbf{C}_m : (\epsilon_{m1} - \epsilon_m^{\text{pl}}). \quad (13)$$

The microstructural stress and total strain are computed, and the microstructural stress is homogenized using the Hill–Mandel lemma to obtain the macroscopic stress

$$\sigma_M^0 = \frac{1}{|\Omega|} \int_{\Omega} \sigma_{m1} d\Omega. \quad (14)$$

The macroscopic effective elastic strain ϵ_M^{el} (or plastic strain ϵ_M^{pl}) is then separated from the total strain. According to Eq. (10), the effective macroscopic elastic strain can be expressed as

$$\epsilon_M^{\text{el}} = (\mathbf{C}_M)^{-1} : \sigma_M^0. \quad (15)$$

This is equivalent to applying the homogenized stress from the reference RVE, σ_M^0 , to a second RVE which is identical to the first RVE, except that the material is an undamaged elastic material,

$$\sigma_{m2} = \mathbf{C}_m : \epsilon_{m2}. \quad (16)$$

The microstructural strain in the second RVE is computed and homogenized to yield the macroscopic elastic strain as

$$\epsilon_M^{el} = \frac{1}{|\Omega|} \int_{\Omega} \epsilon_{m2} d\Omega. \quad (17)$$

Finally, the macroscopic stress of the damaged material can be computed based on Eq. (9)

$$\sigma_M^d = \mathbf{C}_M^d : \epsilon_M^{el}. \quad (18)$$

This is equivalent to applying the homogenized strain from the second RVE, ϵ_M^{el} , to a third RVE with damaged elastic material properties,

$$\sigma_{m3} = (1 - d_m) \mathbf{C}_m : \epsilon_{m3}, \quad (19)$$

where the microscopic damage parameter, d_m , is a function of the state variables, \mathbf{q}_{m1} , in the first RVE or the reference elasto-plastic RVE,

$$d_m = d_m(\mathbf{q}_{m1}). \quad (20)$$

The microscopic stress in the third RVE is computed and homogenized as

$$\sigma_M^d = \frac{1}{|\Omega|} \int_{\Omega} \sigma_{m3} d\Omega. \quad (21)$$

The homogenized stress, σ_M^d , is returned to the macroscale model as the damaged macroscopic stress at the material point corresponding to the macroscopic strain.

2.4. Effective damage parameter

To characterize the damage state of the RVE, an effective macroscopic damage parameter, d_M , can be defined as

$$d_M = 1 - \frac{\|\sigma_M^d : \sigma_M^0\|}{\|\sigma_M^0 : \sigma_M^0\|}. \quad (22)$$

The macroscale homogenized material and the associated RVE are said to be fully damaged when $d_M = 1$. Note that the effective damage parameter is not defined as the field average of the local damage parameter, so full damage can be achieved even if only part of the RVE is fully damaged. The effective damage parameter is a natural by-product of the homogenization scheme and does not affect the stress–strain relation, but it does provide a useful state variable/indicator for tracking localization in the macroscale simulation.

3. Non-local macroscopic damage

A non-local macroscale damage model is adopted to deal with the pathological mesh dependence due to strain softening. The macroscopic damage is based on the microscale damage computed using the proposed micro-damage algorithm from Section 2.3. The algorithm captures the complex damage mechanisms due to material heterogeneities at the microstructural level without predefining the form or requiring a length scale. This is achieved at a local macroscopic point by homogenizing the damaged stress computed in the microscale RVE. Although the microscale damage model does not require a non-local length scale, the macroscale model is still subject to the pathological mesh dependence when the homogenized results from the RVE are passed back to the macroscale material point.

A non-local macroscopic length scale is introduced via a convolution integral. The non-local microscale damage parameter, \tilde{d}_m , at point \mathbf{x} inside the RVE is obtained as a weighted average over a spatial neighborhood of the macroscale point ξ under consideration,

$$\tilde{d}_m(\mathbf{x}, \xi) = \int_B \omega(\|\xi - \xi'\|) d_m(\mathbf{x}, \xi') d\xi', \quad (23)$$

where $d_m(\mathbf{x}, \xi')$ is the local damage increment at a microscale point \mathbf{x} inside the RVE associated with macroscale point ξ' . Note that the non-local regularization can also be performed on other variables, such as strain, stress and effective plastic strain.

The clustering domain decomposition utilized for the reduced order SCA method in Section 4 leads to a discrete form of the convolution integral. The non-local damage parameter in the I th cluster \tilde{d}_m^I at point ξ of a reduced order RVE can be written as

$$\tilde{d}_m^I(\xi) = \int_B \omega(\|\xi - \xi'\|) d_m^I(\xi') d\xi', \quad (24)$$

where $d_m^I(\xi')$ is the local damage parameter in the I th cluster of the reduced RVE at point ξ' .

The non-local weighting function $\omega(\|\xi - \xi'\|)$ is normalized to preserve a uniform field,

$$\omega(\|\xi - \xi'\|) = \frac{\omega_\infty(\|\xi - \xi'\|)}{\int_B \omega_\infty(\|\xi - \xi'\|) d\xi'}, \quad (25)$$

where B denotes the macroscale support domain for the non-local integration. One possible weighting function, which is utilized for the examples in this paper, is a polynomial bell function with compact support [7],

$$\omega_\infty(r) = \left\langle 1 - \frac{4r^2}{l_0^2} \right\rangle^2, \quad (26)$$

where the Macauley brackets $\langle \dots \rangle$ are defined as $\langle x \rangle = \max(x, 0)$, and l_0 is the macroscale length scale parameter. Since $\omega_\infty(r)$ vanishes for $r > l_0/2$, the support domain B is circular in two-dimensions, or spherical in three-dimensions, with a radius $l_0/2$.

The macroscale length parameter, l_0 , determines the width of the damage localization band, and limits localization to ensure numerical convergence to a physically meaningful solution. The non-local microscale damage parameter \tilde{d}_m (or \tilde{d}_m^I) is utilized in the third RVE (see the definition in Section 2.3), resulting in a microscale stress–strain relation in Eq. (19) of

$$\sigma_{m3} = (1 - \tilde{d}_m) \mathbf{C}_m : \epsilon_{m3}. \quad (27)$$

For the new micro-damage homogenization method with the non-local formulation, the non-local microscale damage parameter \tilde{d}_m is computed in Step 2.c in Box I, and \tilde{d}_m will affect on the macroscale material responses through homogenization of the RVE stress.

The macroscale length parameter l_0 can be determined by measuring the width of the strain localization band, either in high-fidelity direct numerical simulations (DNS) which model the damage evolution process explicitly [2,8,9], or by experimental image post-processing using digital image correlation (DIC) analysis [49]. For a given weighting function defined by l_0 , the mesh size l_e of the macroscale model (e.g. FEM) needs to be small enough to effectively remove the mesh sensitivity and reduce the error caused by sample aliasing [50,51]. In this paper, $l_e < l_0/4$ is used, and the influence of mesh size will also be investigated in Section 6.1.

4. Self-consistent clustering analysis: model reduction

The concurrent multiscale modeling framework for the micro-damage algorithm is applicable to complex materials, but additional computational resources are needed to solve the microscale model at each integration point. As a result, the whole concurrent simulation is prohibitively expensive for complex microscale representation.

The self-consistent clustering analysis (SCA) with a new projection-based self-consistent scheme is proposed to increase the efficiency of the concurrent calculations. The efficiency of SCA is achieved via data compression algorithms which group local microstructures into clusters during an offline training stage. Grouping material points with similar mechanical behavior into clusters results in significantly fewer degrees of freedom than the original DNS; the computational speed is thus greatly improved. The self-consistent scheme introduced in the online stage of SCA guarantees the accuracy of the reduced order model. Importantly, SCA is valid for any local nonlinear constitutive law (such as plasticity and damage) of each material phase in the microscale model.

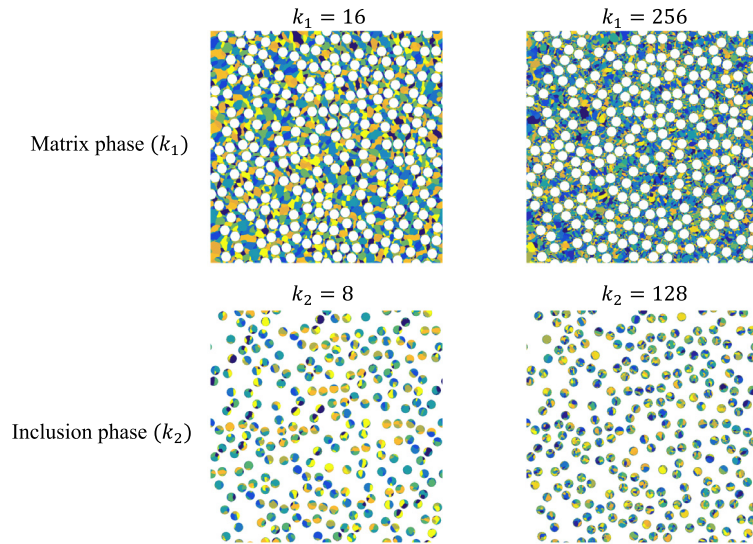


Fig. 4. k-means clustering results of the cross-section of a two-dimensional RVE with circular inclusions. The high-fidelity RVE is discretized by a 1200×1200 mesh. Each cluster contains all the separate sub-domains with the same color. (For interpretation of the references to color in this figure legend, the reader is referred to the web version of this article.)

4.1. Offline stage: mechanistic material characterization

Grouping material points with similar mechanical behavior into a single cluster is performed by domain decomposition of the material points using the clustering methods [52]. First, the similarity between two material points is measured by the strain concentration tensor $\mathbf{A}_m(\mathbf{x})$, which is defined as

$$\boldsymbol{\varepsilon}_m(\mathbf{x}) = \mathbf{A}_m(\mathbf{x}) : \boldsymbol{\varepsilon}_M \quad \text{in } \Omega, \quad (28)$$

where $\boldsymbol{\varepsilon}_M$ is the elastic macroscopic strain corresponding to the boundary conditions on the RVE, and $\boldsymbol{\varepsilon}_m(\mathbf{x})$ is the elastic local strain at point \mathbf{x} in the microscale RVE domain Ω . In a two-dimensional (2D) model, $\mathbf{A}_m(\mathbf{x})$ has 9 independent components, which can be determined by a set of elastic DNS calculations under 3 orthogonal loading conditions. For a linear elastic material, the strain concentration tensor is independent of the loading conditions. Other metrics, such as effective plastic strain and damage parameter, can also be selected for the offline data clustering, but may require extra computation in the offline stage.

After computing the strain concentration tensor $\mathbf{A}_m(\mathbf{x})$, the k-means clustering method [53] is used to group data points. Additional details about the clustering algorithm are provided in [Appendix A](#). Since all the material points in a cluster are assumed to have the same mechanical responses, the number of the degrees of freedom is significantly reduced through this compression/clustering step. The k-means clustering results of a 2D heterogeneous RVE in the matrix phase and inclusion phase at two levels of resolution are provided in [Fig. 4](#).

A primary assumption associated with the domain decomposition is that any local variable $\boldsymbol{\beta}(\mathbf{x})$ is uniform within each cluster. Globally, this is equivalent to having a piece-wise uniform profile of the variable in the RVE. This piecewise uniform approximation enables us to reduce the number of degrees of freedom for the Lippmann–Schwinger equation, which is solved in the following online stage (see [Section 4.2](#)). Meanwhile, the so-called interaction tensor \mathbf{D}^{IJ} can also be extracted as an invariant inside the reduced Lippmann–Schwinger equation. Details on computing the interaction tensors are provided in [Appendix B](#).

It should be noted that although the domain decomposition is based on a specific selection of elastic properties for each material phase in the offline stage, the same database can be used for predicting responses for new combinations of material constituents in the online stage. Even though the absolute value of the strain concentration tensor $\mathbf{A}_m(\mathbf{x})$ strongly depends on the phase properties, the clustering results are more sensitive to the distribution of $\mathbf{A}_m(\mathbf{x})$ in the RVE, which characterizes the geometrical heterogeneity. In this paper, the same database shown in [Fig. 4](#) is used for predicting the responses of two different RVEs embedded with hard or soft inclusions.

4.2. Online stage: a new projection-based self-consistent scheme

As discussed in [1], the equilibrium condition in the RVE can be rewritten as a continuous Lippmann–Schwinger integral equation by introducing a homogeneous isotropic linear elastic reference material,

$$\Delta \boldsymbol{\varepsilon}_m(\mathbf{x}) + \int_{\Omega} \boldsymbol{\Phi}^0(\mathbf{x}, \mathbf{x}') : [\Delta \boldsymbol{\sigma}_m(\mathbf{x}') - \mathbf{C}^0 : \Delta \boldsymbol{\varepsilon}_m(\mathbf{x}')] d\mathbf{x}' - \Delta \boldsymbol{\varepsilon}^0 = \mathbf{0}, \quad (29)$$

where $\Delta \boldsymbol{\varepsilon}^0$ is the far-field strain increment controlling the evolution of the local strain. The far-field strain is uniform in the RVE. The reference material is isotropic linear elastic, and its stiffness tensor \mathbf{C}^0 can be determined by two independent Lamé parameters λ^0 and μ^0 ,

$$\mathbf{C}^0 = \mathbf{f}(\lambda^0, \mu^0) = \lambda^0 \mathbf{I} \otimes \mathbf{I} + \mu^0 \mathbf{II}, \quad (30)$$

where \mathbf{I} is the second-rank identity tensor, and \mathbf{II} is the symmetric part of the fourth-rank identity tensor. Moreover, $\Delta \boldsymbol{\varepsilon}_m(\mathbf{x})$ and $\Delta \boldsymbol{\sigma}_m(\mathbf{x})$ are the microscopic strain and stress increments, respectively. Averaging the incremental integral equation in Eq. (29) in Ω leads to

$$\frac{1}{|\Omega|} \int_{\Omega} \Delta \boldsymbol{\varepsilon}_m(\mathbf{x}) d\mathbf{x} + \frac{1}{|\Omega|} \int_{\Omega} \left[\int_{\Omega} \boldsymbol{\Phi}^0(\mathbf{x}, \mathbf{x}') d\mathbf{x} \right] : [\Delta \boldsymbol{\sigma}_m(\mathbf{x}') - \mathbf{C}^0 : \Delta \boldsymbol{\varepsilon}_m(\mathbf{x}')] d\mathbf{x}' - \Delta \boldsymbol{\varepsilon}^0 = \mathbf{0}. \quad (31)$$

Using the boundary conditions for deriving the Green's function, Eq. (B.5) can be equivalently written in the spatial domain as

$$\int_{\Omega} \boldsymbol{\Phi}^0(\mathbf{x}, \mathbf{x}') d\mathbf{x} = \mathbf{0}. \quad (32)$$

Substituting Eq. (32) into (31) gives

$$\Delta \boldsymbol{\varepsilon}^0 = \frac{1}{|\Omega|} \int_{\Omega} \Delta \boldsymbol{\varepsilon}_m(\mathbf{x}) d\mathbf{x}, \quad (33)$$

which indicates that the far-field strain increment is always equal to the ensemble averaged strain increment in the RVE. To compute the strain increment $\Delta \boldsymbol{\varepsilon}_m(\mathbf{x})$ in the integral Eq. (29), constraints are needed from the macroscopic boundary conditions. For the homogenization scheme proposed in Section 2, two types of constraints are used: (1) macro-strain constraints in RVEs 1 and 3

$$\frac{1}{|\Omega|} \int_{\Omega} \Delta \boldsymbol{\varepsilon}_m(\mathbf{x}) d\mathbf{x} = \Delta \boldsymbol{\varepsilon}_M \quad \text{or} \quad \Delta \boldsymbol{\varepsilon}^0 = \Delta \boldsymbol{\varepsilon}_M; \quad (34)$$

and (2) a macro-stress constraint in RVE 2

$$\frac{1}{|\Omega|} \int_{\Omega} \boldsymbol{\sigma}_m(\mathbf{x}) d\mathbf{x} = \boldsymbol{\sigma}_M. \quad (35)$$

For more general cases, macro-stress and mixed constraints can also be formulated [1]. Here the boundary conditions are applied as constraints on the volume averages of strain or stress inside the RVE. This methodology differs from the standard finite element method in which the boundary conditions constrain the displacement or force at the RVE boundaries.

As the full-field calculations (e.g. FFT-based method) of the continuous Lippmann–Schwinger equation may require excessive computational resources, the discretization of the integral equation is performed based on the domain decomposition in the offline stage. With the piecewise uniform assumption in Eq. (58), the number of degrees of freedom and the number of the internal variables in the new system can be reduced. After decomposition, the discretized integral equation of the I th cluster can be derived as

$$\Delta \boldsymbol{\varepsilon}_m^I + \sum_{J=1}^k \mathbf{D}^{IJ} : [\Delta \boldsymbol{\sigma}_m^J - \mathbf{C}^0 : \Delta \boldsymbol{\varepsilon}_m^J] - \Delta \boldsymbol{\varepsilon}^0 = \mathbf{0}, \quad (36)$$

where $\Delta \boldsymbol{\varepsilon}_m^J$ and $\Delta \boldsymbol{\sigma}_m^J$ are the microscopic strain and stress increment in the J th cluster. The interaction tensor, \mathbf{D}^{IJ} , is defined in Eq. (B.1), and is related to the Green's function of the reference material. After the discretization, the far field strain is still equal to the average strain in the RVE,

$$\Delta \boldsymbol{\varepsilon}^0 = \sum_{I=1}^k c^I \Delta \boldsymbol{\varepsilon}_m^I, \quad (37)$$

where c^I is the volume fraction of the I th cluster. Meanwhile the macroscopic boundary conditions are also required to be discretized. For instance, the discrete form of the macro-strain constraint can be written as

$$\sum_{I=1}^k c^I \Delta \boldsymbol{\epsilon}_m^I = \Delta \boldsymbol{\epsilon}_M \quad \text{or} \quad \Delta \boldsymbol{\epsilon}^0 = \Delta \boldsymbol{\epsilon}_M. \quad (38)$$

Similarly, the discretized macro-stress constraint becomes

$$\sum_{I=1}^k c^I \Delta \boldsymbol{\sigma}_m^I = \Delta \boldsymbol{\sigma}_M. \quad (39)$$

An important feature of the continuous Lippmann–Schwinger in Eq. (29) is that its solution is independent of the choice of the reference material \mathbf{C}^0 . This can be explained by the fact that the physical problem is fully described by the equilibrium condition and the prescribed macroscopic boundary conditions. However, once the equation is discretized based on the piecewise uniform assumption, the equilibrium condition is not strictly satisfied at every point in the RVE, and the solution of the reduced system depends on the choices of \mathbf{C}^0 . This discrepancy can be reduced by increasing the number of clusters into the system, but with a computational cost increase due to the increased degrees of freedom.

To achieve both efficiency and accuracy, a self-consistent scheme is used in the online stage, which shows good accuracy with fewer clusters. In the self-consistent scheme, the stiffness tensor of the reference material \mathbf{C}^0 is set approximately the same as the homogenized stiffness tensor $\bar{\mathbf{C}}$,

$$\mathbf{C}^0 \rightarrow \bar{\mathbf{C}}. \quad (40)$$

The homogenized stiffness tensor $\bar{\mathbf{C}}$ of the RVE can be expressed as

$$\bar{\mathbf{C}} = \sum_{I=1}^k c^I \mathbf{C}_{\text{alg}}^I : \mathbf{A}_m^I, \quad (41)$$

where $\mathbf{C}_{\text{alg}}^I$ is the algorithm stiffness tensor of the material in the I th cluster and is an output of the local constitutive law for the current strain increment in the cluster,

$$\mathbf{C}_{\text{alg}}^I = \frac{\partial \Delta \boldsymbol{\sigma}_m^I}{\partial \Delta \boldsymbol{\epsilon}_m^I}. \quad (42)$$

The strain concentration tensor of the I th cluster \mathbf{A}_m^I relates the local strain increment in the I th cluster $\Delta \boldsymbol{\epsilon}_m^I$ to the far-field strain increment $\Delta \boldsymbol{\epsilon}^0$,

$$\Delta \boldsymbol{\epsilon}_m^I = \mathbf{A}_m^I : \Delta \boldsymbol{\epsilon}^0. \quad (43)$$

The strain concentration tensor \mathbf{A}_m^I can be determined by first linearizing the discretized integral equation (36) using $\mathbf{C}_{\text{alg}}^I$ and then inverting the Jacobian matrix of the Newton's method. Since $\bar{\mathbf{C}}$ is only required for the self-consistent scheme, the calculation of $\bar{\mathbf{C}}$ is only performed once after the convergence of the Newton's method to save the computational cost.

Due to the nonlinearity of the material responses, such as plasticity, it is usually not possible to determine an isotropic \mathbf{C}^0 which provides an exact match with $\bar{\mathbf{C}}$. In [1], the self-consistent scheme is formulated as an optimization problem, where the optimum isotropic \mathbf{C}^0 minimizes the error between the predicted average stress increments. Although this scheme does not require computing $\bar{\mathbf{C}}$ explicitly, it has mainly two drawbacks. First, the optimization problem is under-determined under pure shear or hydrostatic loading conditions, so that one of two independent elastic constants need to be estimated. More importantly, the modulus of the optimum reference material may become negative under complex loading conditions, which is deleterious to the convergence of the fixed-point method.

In this paper, a new self-consistent scheme is proposed based on projection of the effective stiffness tensor $\bar{\mathbf{C}}$, which is formulated as two well-defined optimization problems. For a 2D plane strain problem, the stiffness tensor of the isotropic reference material \mathbf{C}_{pe}^0 is decomposed as

$$\mathbf{C}_{iso}^0 = 2\kappa^0 \mathbf{J} + 2\mu^0 \mathbf{K}, \quad (44)$$

where the 2D bulk modulus can be related to the Lamé parameters,

$$\kappa^0 = \lambda^0 + \mu^0. \quad (45)$$

The fourth-rank tensor \mathbf{J} and \mathbf{K} are defined as

$$\mathbf{J} = \frac{1}{2} (\mathbf{I} \otimes \mathbf{I}) \quad \text{and} \quad \mathbf{K} = \mathbf{II} - \mathbf{J}, \quad (46)$$

where \mathbf{I} is the second-rank identity tensor, \mathbf{II} is the fourth-rank symmetric identity tensor. It can be shown that \mathbf{J} and \mathbf{K} are orthogonal to each other,

$$\mathbf{J} :: \mathbf{K} = 0, \quad (47)$$

and

$$\mathbf{J} :: \mathbf{J} = 1, \quad \mathbf{K} :: \mathbf{K} = 2, \quad (48)$$

where “::” denotes the inner product between two fourth-order tensors, or $\mathbf{A} :: \mathbf{B} = A_{ijkl} B_{ijkl}$.

To find the optimum κ^0 and μ^0 from the projection of the effective stiffness tensor $\bar{\mathbf{C}}$, two optimization problems are defined

$$\kappa^0 = \underset{\{\kappa'\}}{\operatorname{argmin}} \left\| [\bar{\mathbf{C}} - \mathbf{C}_{iso}(\kappa')] : \Delta \boldsymbol{\varepsilon}_h^0 \right\|^2 \quad (49)$$

and

$$\mu^0 = \underset{\{\mu'\}}{\operatorname{argmin}} \left\| [\bar{\mathbf{C}} - \mathbf{C}_{iso}(\mu')] : \Delta \boldsymbol{\varepsilon}_d^0 \right\|^2, \quad (50)$$

where $\Delta \boldsymbol{\varepsilon}_h^0$ and $\Delta \boldsymbol{\varepsilon}_d^0$ are the hydrostatic and deviatoric parts of the far-field strain increment $\Delta \boldsymbol{\varepsilon}^0$. By taking the derivative of the cost functions in Eqs. (49) and (50) for finding the stationary points, the optimum κ^0 and μ^0 can be expressed in Voigt notation as

$$\kappa^0 = \frac{\bar{\mathbf{C}}_{11} + \bar{\mathbf{C}}_{12} + \bar{\mathbf{C}}_{21} + \bar{\mathbf{C}}_{22}}{4} \quad (51)$$

and

$$\mu^0 = \eta_1 \left(\frac{\bar{\mathbf{C}}_{11} - \bar{\mathbf{C}}_{12} - \bar{\mathbf{C}}_{21} + \bar{\mathbf{C}}_{22}}{4} \right) + (1 - \eta_1) \bar{\mathbf{C}}_{33} + \eta_2 (\bar{\mathbf{C}}_{13} - \bar{\mathbf{C}}_{23} - \bar{\mathbf{C}}_{32} + \bar{\mathbf{C}}_{31}), \quad (52)$$

with

$$\eta_1 = \frac{(\Delta \varepsilon_{11}^0 - \Delta \varepsilon_{22}^0)^2}{(\Delta \varepsilon_{11}^0 - \Delta \varepsilon_{22}^0)^2 + (\Delta \gamma_{12}^0)^2}, \quad \eta_2 = \frac{(\Delta \varepsilon_{11}^0 - \Delta \varepsilon_{22}^0) \Delta \gamma_{12}^0}{(\Delta \varepsilon_{11}^0 - \Delta \varepsilon_{22}^0)^2 + (\Delta \gamma_{12}^0)^2}. \quad (53)$$

For cases when the denominator $(\Delta \varepsilon_{11}^0 - \Delta \varepsilon_{22}^0)^2 + (\Delta \gamma_{12}^0)^2$ vanishes, $\eta_1 = 0.5$ and $\eta_2 = 0$ are used. Specifically, if the effective macroscopic material is orthotropic, the third term in Eq. (52) can be dismissed. Similarly, this self-consistent scheme can also be extended to 3D materials. The expressions of κ^0 and μ^0 for the 3D self-consistent scheme are derived based on Eq. (49) and (50).

$$\kappa^0 = \frac{\bar{\mathbf{C}}_{11} + \bar{\mathbf{C}}_{12} + \bar{\mathbf{C}}_{13} + \bar{\mathbf{C}}_{21} + \bar{\mathbf{C}}_{22} + \bar{\mathbf{C}}_{23} + \bar{\mathbf{C}}_{31} + \bar{\mathbf{C}}_{32} + \bar{\mathbf{C}}_{33}}{9} \quad (54)$$

and

$$\mu^0 = \frac{\Delta \boldsymbol{\varepsilon}_d^0 : \bar{\mathbf{C}} : \Delta \boldsymbol{\varepsilon}_d^0}{\Delta \boldsymbol{\varepsilon}_d^0 : \mathbf{T} : \Delta \boldsymbol{\varepsilon}_d^0}, \quad (55)$$

where \mathbf{T} is a transformation tensor derived from the optimum problem. It can be written in Voigt notation as

$$\mathbf{T} = \begin{Bmatrix} 4/3 & -2/3 & -2/3 & 0 & 0 & 0 \\ -2/3 & 4/3 & -2/3 & 0 & 0 & 0 \\ -2/3 & -2/3 & 4/3 & 0 & 0 & 0 \\ 0 & 0 & 0 & 1 & 0 & 0 \\ 0 & 0 & 0 & 0 & 1 & 0 \\ 0 & 0 & 0 & 0 & 0 & 1 \end{Bmatrix}. \quad (56)$$

Eqs. (52) and (55) show that the optimum shear modulus, μ^0 , is weighted by the loading direction, which helps to capture the hardening effect on the stiffness tensor. This improves the accuracy of the self-consistent scheme, as compared to simply determining κ^0 and μ^0 by minimizing the distance between the stiffness tensors \mathbf{C}_{iso}^0 and $\bar{\mathbf{C}}$, which would correspond to averaging the optimum shear modulus in all directions. The algorithm of the self-consistent scheme is shown in Box I in a general sense. For nonlinear materials, the stress increment $\Delta\sigma_m^J$ is a nonlinear function of its strain increment $\Delta\epsilon_m^J$, and Newton's method is normally used to solve the nonlinear system iteratively at each load increment. Additional details on the Newton's iteration are provided in [Appendix C](#).

Box I General algorithm for the self-consistent scheme

1. Initial conditions and initialization: set (κ^0, μ^0) ; $n = 0$; $\{\Delta\epsilon_m^I, \Delta\epsilon^0\}_n = \mathbf{0}$
2. For loading increment $n + 1$, update the interaction tensor \mathbf{D}^{IJ} and the stiffness tensor of the reference material \mathbf{C}^0 based on (κ^0, μ^0)
3. Solve the discretized Lippmann–Schwinger equation (36). For nonlinear materials, Newton's method is used.
4. Compute the effective stiffness tensor $\bar{\mathbf{C}}$, and calculate the optimum (κ^0, μ^0) using Eqs. (51) and (52) (2D plane strain)
5. Check error criterion for (κ^0, μ^0) ; if not met, go to 2
6. Update the strain and stress increments: $\{\Delta\epsilon_m^I, \Delta\epsilon^0\}_{n+1}, \{\Delta\sigma_m^I\}_{n+1}$
7. Update the index of loading increment: $n \leftarrow n + 1$
8. If simulation not complete, go to 2.

5. Microscale elasto-plastic RVE with damage

Numerical examples are presented to investigate and demonstrate the performance of the micro-damage algorithm combined with an SCA reduced order model. A detailed study is performed at the microscale RVE level to investigate the effect of RVE size, and to validate the RVE predictions from the SCA model against high-fidelity direct numerical simulations (DNS) with the finite element method and the FFT-based method using a fine mesh and periodic boundary conditions. The computational efficiency of the proposed method is also discussed.

5.1. Material properties and damage parameters

Self-consistent clustering analysis (SCA) is applied for the homogenization analysis of a nonlinear elasto-plastic heterogeneous material with damage under 2D plane strain conditions. As shown in [Fig. 5](#), an RVE is created with multiple identical circular inclusions (phase 2) embedded in the matrix (phase 1). The volume fraction of the inclusion phase is 30%. In practice, the microstructural morphology of the RVE can be obtained from imaging techniques (e.g. scanning electron microscope and focus ion-beam) or computational reconstruction. For SCA results comparison and validation, the problem is initially solved using a 1200×1200 DNS model with sides of length $2L$ and periodic boundary conditions.

To develop the material clustering database in the offline stage of SCA, linear elastic material properties are used for the phase 1 and phase 2 materials:

$$E_1 = 100 \text{ GPa}, \nu_1 = 0.3; \quad E_2 = 500 \text{ GPa}, \nu_2 = 0.19 \quad (57)$$

where the subscripts 1 and 2 refer to the matrix phase and inclusion phase, respectively. The clustering results based on the material properties in Eq. (57) are shown in [Fig. 4](#). The number of phase 1 clusters is denoted as k_1 , and the

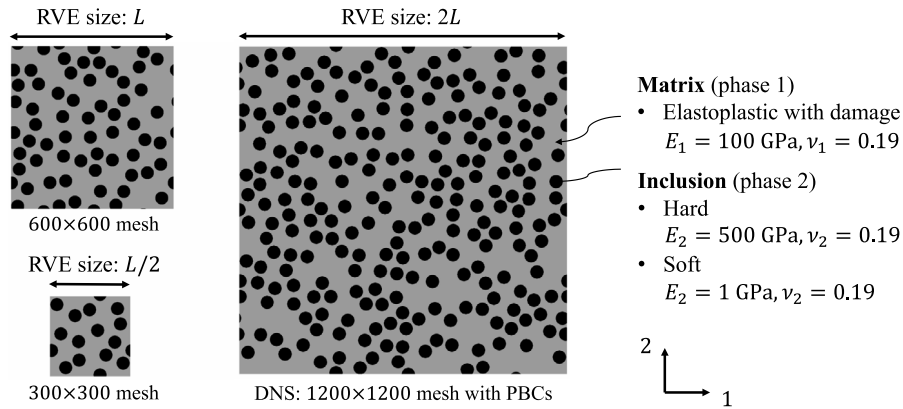


Fig. 5. Illustration of the microscale RVE of a two-phase heterogeneous material used for the analysis: matrix (phase 1) with randomly distributed circular inclusions (phase 2) embedded. The DNS with 1200×1200 FE mesh has 1.44 million 4-node linear plane strain element with reduced integration.

number of phase 2 clusters is denoted as k_2 . The ratio between k_1 and k_2 is defined according to the phase volume fractions. For the composite material used in this paper, the number of clusters in phase 2 is chosen as approximately half the number of clusters in phase 1 ($k_2 = \lceil k_1/2 \rceil$), since the volume fraction of phase 2 is 30%. It will be shown in Sections 5.3 and 5.4 that it is possible to use the same material database with the same RVE geometry but different phase properties.

After forming the material database, different material properties for the constituent materials can be evaluated. The matrix phase is modeled as an elasto-plastic material which undergoes damage. Its local constitutive law is given in Eq. (5) and an associative plastic flow law with a von Mises yield surface is considered. The yield stress σ_Y is determined by the hardening law as a function of the effective plastic strain $\bar{\epsilon}^{pl}$, which is a monotonically increasing internal state variable of the plastic material during the deformation. The yielding stress σ_Y^0 is equal to 0.5 GPa. The hardening law is considered to be piecewise linear and isotropic,

$$\sigma_Y(\bar{\epsilon}^{pl}) = \begin{cases} 0.5 + 5\bar{\epsilon}^{pl} & \bar{\epsilon}^{pl} \in [0, 0.04) \\ 0.7 + 2\bar{\epsilon}^{pl} & \bar{\epsilon}^{pl} \in [0.04, \infty) \end{cases} \text{ GPa.} \quad (58)$$

The inclusions remain as a linear elastic material, but either hard or soft inclusions can be considered by making the Young's modulus of the inclusions either harder or softer than the matrix phase. For these two cases, the properties of the inclusion phase evaluated are

$$E_2 = 500 \text{ GPa}, \nu_2 = 0.19 \quad \text{hard inclusions,} \quad (59)$$

and

$$E_2 = 1 \text{ GPa}, \nu_2 = 0.19 \quad \text{soft inclusions.} \quad (60)$$

Damage evolution is modeled as an exponential function of the effective plastic strain,

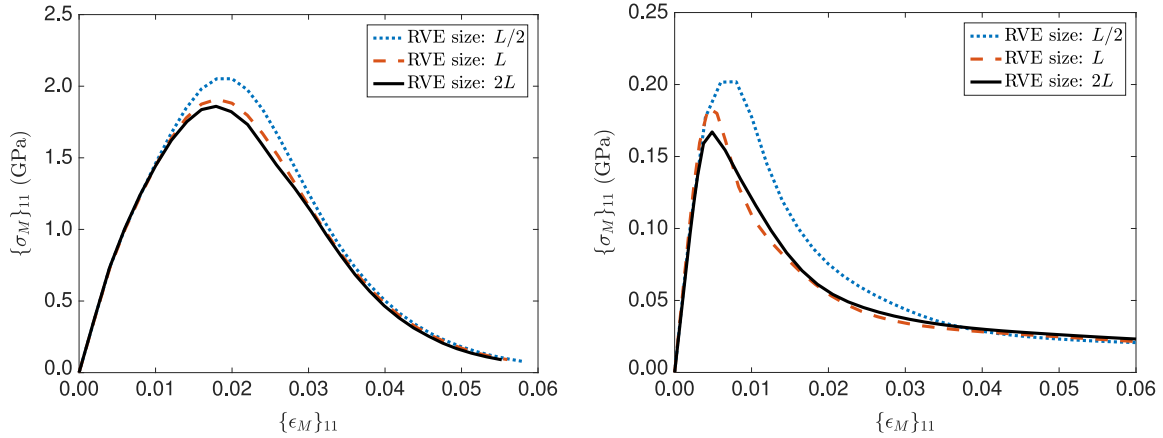
$$d_m(\bar{\epsilon}^{pl}) = \begin{cases} 0 & \text{if } \bar{\epsilon}^{pl} \leq \bar{\epsilon}^{cr} \\ 1 - \frac{\bar{\epsilon}^{cr}}{\bar{\epsilon}^{pl}} \exp(-\alpha(\bar{\epsilon}^{pl} - \bar{\epsilon}^{cr})) & \text{if } \bar{\epsilon}^{pl} > \bar{\epsilon}^{cr} \end{cases} \quad (61)$$

where α is an evolution rate parameter and $\bar{\epsilon}^{cr}$ is the critical effective plastic strain at damage initiation. Since the damage process is irreversible, $\alpha \geq 0$. If $\alpha = 0$, the material is purely elasto-plastic with no damage. For positive α , a fully damaged condition ($d_m = 1$) will be achieved at a finite effective plastic strain. Unless otherwise stated, the baseline damage properties used in this section are $\alpha = 100$ and $\bar{\epsilon}^{cr} = 0.02$. The material parameters of the RVE are summarized in Table 1.

Table 1

Material parameters of the microscale elasto-plastic RVE with damage.

E_1 (GPa)	ν_1	E_2 (hard) (GPa)	E_2 (soft) (GPa)
100	0.3	500	1
ν_2	σ_Y^0 (GPa)	α (default)	$\bar{\varepsilon}^{cr}$ (default)
0.3	0.5	100	0.02

**Fig. 6.** The DNS results for the micro-damage algorithm of a damaged RVE with hard inclusions (left) and soft inclusions (right) under uniaxial loading. Three different RVE sizes are investigated: $L/2$, L , and $2L$.

5.2. RVE size and the stabilized micro-damage algorithm

The effect of RVE size on the homogenized results is evaluated under uniaxial tension, biaxial tension, and shear loading conditions. A comparison is made between an RVE of size $L/2$, an RVE of size L , and an RVE of size $2L$ (see Fig. 5). Each RVE had the same inclusion radius, volume fraction, and nearest inclusion distance [33]. Three loading directions in terms of the macroscopic strain ε_M are considered:

(1) uniaxial strain condition

$$\{\varepsilon_M\}_{11} = \bar{\varepsilon}, \quad \{\varepsilon_M\}_{22} = 0, \quad \{\varepsilon_M\}_{12} = 0; \quad (62)$$

(2) biaxial strain condition

$$\{\varepsilon_M\}_{11} = \bar{\varepsilon}, \quad \{\varepsilon_M\}_{22} = \bar{\varepsilon}, \quad \{\varepsilon_M\}_{12} = 0; \quad (63)$$

(3) shear strain condition

$$\{\varepsilon_M\}_{11} = \bar{\varepsilon}, \quad \{\varepsilon_M\}_{22} = -\bar{\varepsilon}, \quad \{\varepsilon_M\}_{12} = 0; \quad (64)$$

where $\bar{\varepsilon}$ denotes the magnitude of the macroscopic strain.

For each step in the proposed homogenization scheme of Section 2, the computations are performed using a finite element model with periodic boundary conditions. The homogenized stress–strain curves $\{\sigma_M\}_{11}$ – $\{\varepsilon_M\}_{11}$ for the damaged RVEs are shown in Fig. 6, where the subscript 11 indicates the homogenized values in the 11 direction (direction of uniaxial loading). Inspection of the curves in Fig. 6 reveals some change in the macroscopic responses given by the micro-damage homogenization algorithm, but the response with damage is not overly sensitive to the RVE size.

The material toughness U_T is defined as the energy per unit volume absorbed before material failure due to load in a fixed loading direction. In a one-dimensional case, the material toughness is simply the area under a stress–strain

Table 2

Comparison of the toughness U_T obtained using DNS for RVE sizes $L/2$, L , and $2L$. Value in parenthesis indicates relative difference to the corresponding prediction from RVE with size $2L$. Toughness units are GJ/m^3 .

RVE Size	Hard inclusions			Soft inclusions		
	Uniaxial	Biaxial	Shear	Uniaxial	Biaxial	Shear
$2L$	0.0735	0.3072	0.0103	0.0046	0.0049	0.0068
L	0.0749(1.9%)	0.3184(3.6%)	0.0104(1.0%)	0.0044(4.3%)	0.0049(0.5%)	0.0070(2.9%)
$L/2$	0.0829(12.7%)	0.3240(5.4%)	0.0111(7.8%)	0.0056(21.7%)	0.0060(22.4%)	0.0075(10.3%)

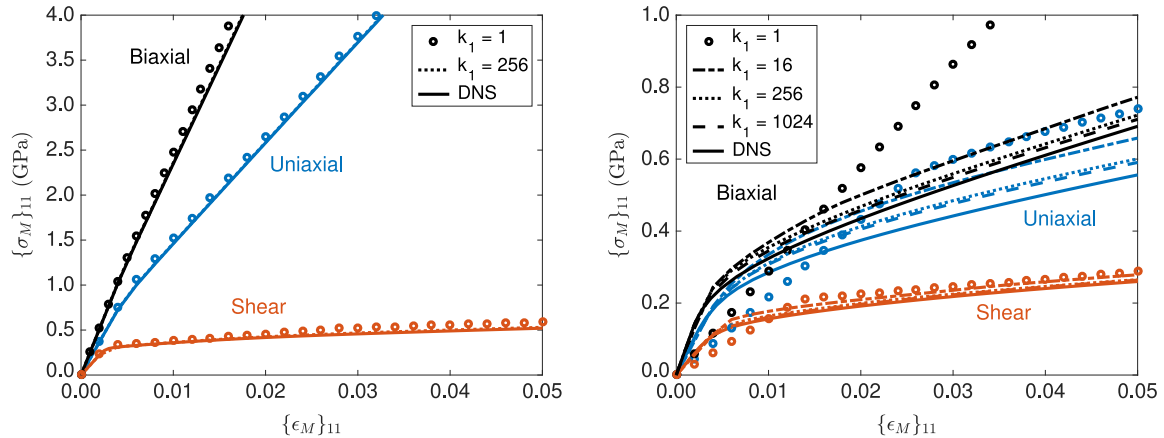


Fig. 7. The stress–strain curves of the undamaged RVE with hard inclusions (left) and soft inclusions (right). Three macro-strain loading conditions are considered: uniaxial loading (blue), biaxial loading (black) and shear loading (red). The solid lines represent the DNS results for comparison (For interpretation of the references to color in this figure legend, the reader is referred to the web version of this article.).

curve. In general, this is expressed mathematically as

$$U_T = \int_0^{\epsilon_M^f} \sigma_M^d d\epsilon_M, \quad (65)$$

where ϵ_M^f is the failure strain for a fully damaged material ($d_M = 0.99$ is used as the failure strain in this calculation). The tabulated results in Table 2 show that the relative difference of the material toughness decreases with increasing RVE size. The homogenized results are not sensitive to the RVE size, which validates the existence of the RVE. Therefore, it provides an effective material damage model for a macroscale material point within a concurrent simulation.

5.3. SCA for an RVE with hard/soft inclusions without material damage

The SCA reduced order method is first applied to an elasto-plastic RVE without considering material damage. The material clustering database is determined in the offline stage using hard inclusions.

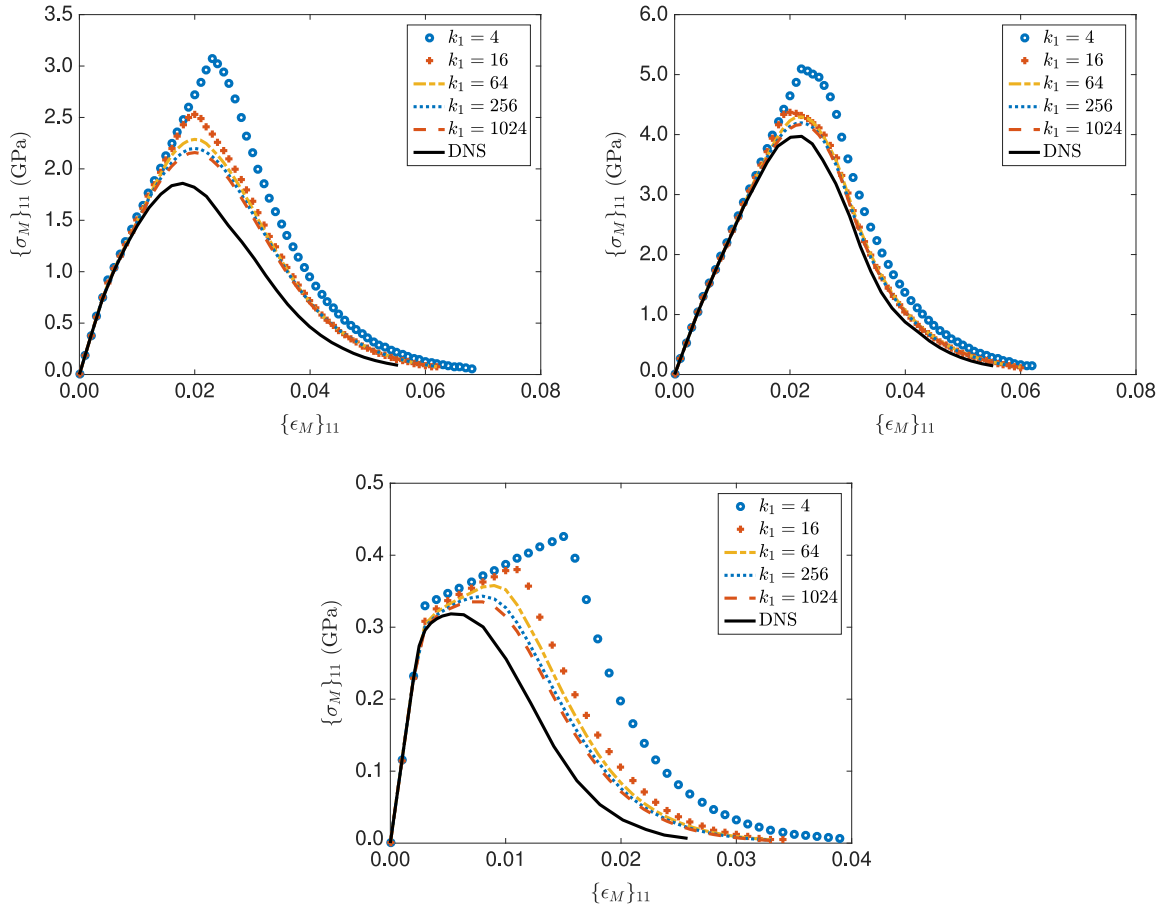
Three loading directions in terms of the macroscopic strain are considered: (1) uniaxial tension, (2) biaxial tension, and (3) shear. The homogenized stress strain curves in the 11 direction ($\{\sigma_M\}_{11} - \{\epsilon_M\}_{11}$) of the undamaged RVE with hard inclusions are presented on the lefthand side of Fig. 7. The numbers of clusters considered in material phase 1 are 1 and 256, and the corresponding DNS results are plotted as the solid lines for comparison. These results show that the SCA predictions under all the three macro-strain constraints are quite accurate, even with only a single cluster in phase 1.

For soft inclusions, it is not possible to achieve the same accuracy with the same number clusters. The right-hand side of Fig. 7 shows that $k_1 = 1$ is not sufficient to capture the stress–strain relation in the elastic or plastic regimes, especially for the uniaxial and biaxial loading conditions. This observation is consistent with the fact that the self-consistent theory in analytical micromechanics methods tends to underestimate the stiffness of porous materials. Nevertheless, by increasing the resolution in the RVE, good agreement with the DNS results can still be achieved, and with significantly fewer degrees of freedom than required by DNS.

Table 3

Computational time of the RVE homogenization of various numbers of clusters on one Intel i7-3632 processor.

k_1	1	4	16	64	256	1024	DNS time
Wall clock time (s)	0.23	0.35	0.80	2.5	11.2	117.8	7814
Speedup of SCA	3.4×10^4	2.2×10^4	9.8×10^3	3.1×10^3	698	66	NA

**Fig. 8.** The stress–strain curves of the damaged RVE with hard inclusions for uniaxial tension, biaxial tension, and shear loading.

Again, it should be emphasized that although the SCA database is created based on the RVEs with hard inclusions (see Eq. (57)), it is valid for other RVEs with the same morphology but different combinations of material properties. As a result, the SCA database (clusters and the interaction tensor \mathbf{D}^{IJ}) can be regarded as a microstructural database which characterizes the geometric heterogeneity of the material and enables the online reduced-order calculation.

The computational cost comparison in Table 3 shows that a typical two-dimensional DNS calculation with a 1200×1200 mesh and 50 loading increments requires 7814 s (≈ 130 min) on one Intel i7-3632 processor, while the online stage of SCA (programmed in MATLAB) took 0.35 s, 2.5 s, 117.8 s on one Intel i7-3632 processor for $k_1 = 4$, $k_1 = 64$ and $k_1 = 1024$, respectively.

5.4. SCA for an RVE with hard/soft inclusions and material damage

The SCA reduced order method is next applied to the same elasto-plastic RVE with hard and soft inclusions. The matrix phase of the RVE is allowed to undergo material damage, which is computed using the micro-damage algorithm in Section 2 and the damage evolution law in Eq. (61).

The homogenized stress–strain results computed using both DNS and SCA with material damage are shown in Fig. 8 for hard inclusions and Fig. 9 for soft inclusions. Results are presented for uniaxial tension loading, biaxial

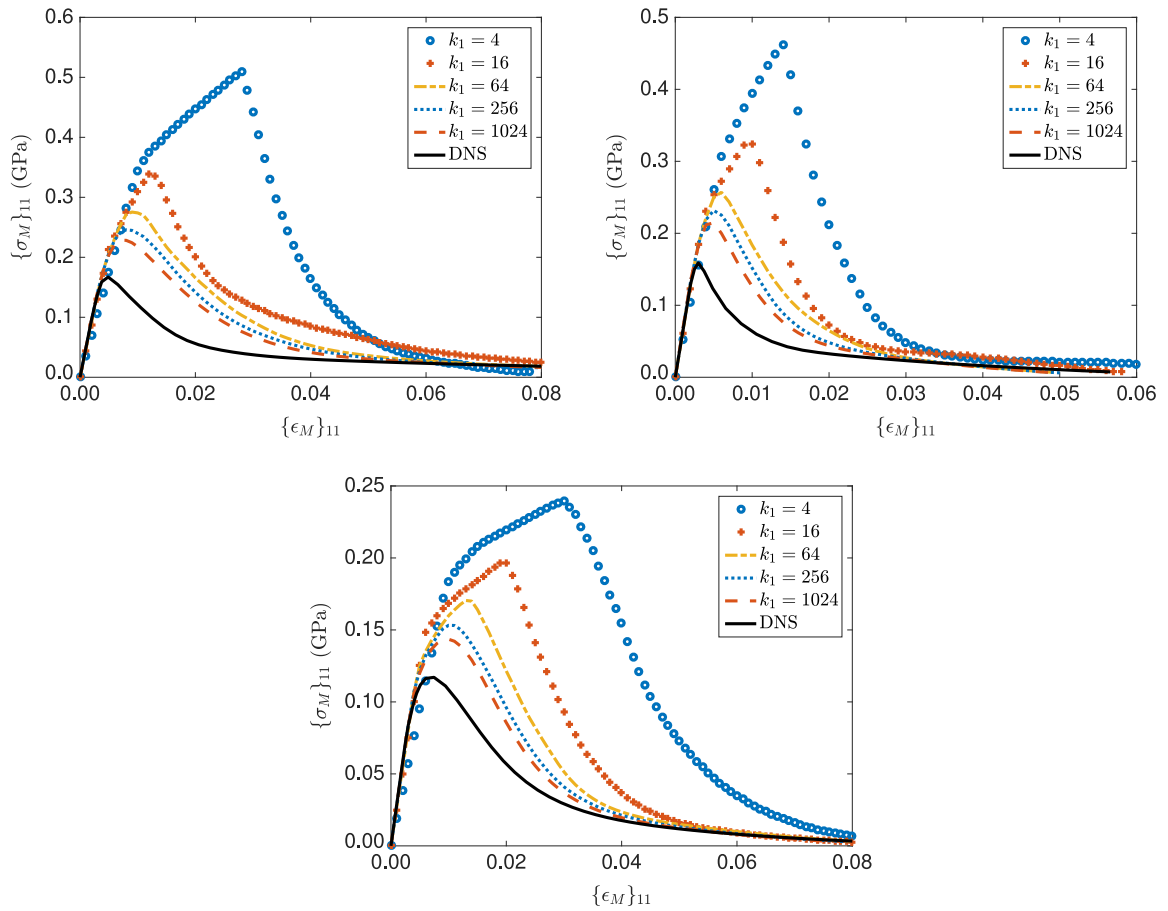


Fig. 9. The stress–strain curves of the damaged RVE with soft inclusions for uniaxial tension, biaxial tension, and shear loading.

tension loading, and shear loading. With the same level of discretization, the SCA predictions with material damage considered do not exhibit the same level of accuracy as the SCA predictions without considering material damage (see Fig. 7). The clustering algorithm was noted to be stiffer than the DNS calculation for the number of clusters evaluated. This difference is expected since material damage is a more localized process than plasticity, and more clusters are required for adequate resolution in the damaged region. On the other hand, the clustering result based on linear elastic responses may not be sufficient for capturing highly localized damage behavior, and this issue will be investigated in future work.

For hard inclusions, it can be seen that under biaxial tension loading and shear loading, SCA results matched the peak stresses and damage evolution with very few clusters. For the uniaxial tension loading, the SCA method tends to overpredict the peak stress and damage evolution, meaning that additional clusters may be required. For soft inclusions, the SCA method is capable of capturing the effect of the damage, but tends to overpredict peak stress and damage evolution. This finding is consistent with the findings in the self-consistent micromechanics theory. In Section 5.5, an energy regularization methodology is presented which provides an effective way of calibrating the damage parameters.

The macroscopic material damage behavior can be characterized by the material toughness, U_T , as a function of the strain ratio $\varepsilon_M^R/\varepsilon_M^{avg}$, where ε_M^{avg} and ε_M^R denote the macroscopic normal strain and shear strain, respectively. Due to the isotropy of the RVE considered in this work, the material toughness should be uniquely determined by the loading direction denoted by $\varepsilon_M^R/\varepsilon_M^{avg}$. For a given set of ε_M^{avg} and ε_M^R , the loading condition is defined to be

$$\{\varepsilon_M\}_{11} = \varepsilon_M^{avg}, \{\varepsilon_M\}_{22} = \varepsilon_M^{avg}, \{\varepsilon_M\}_{12} = \varepsilon_M^R. \quad (66)$$

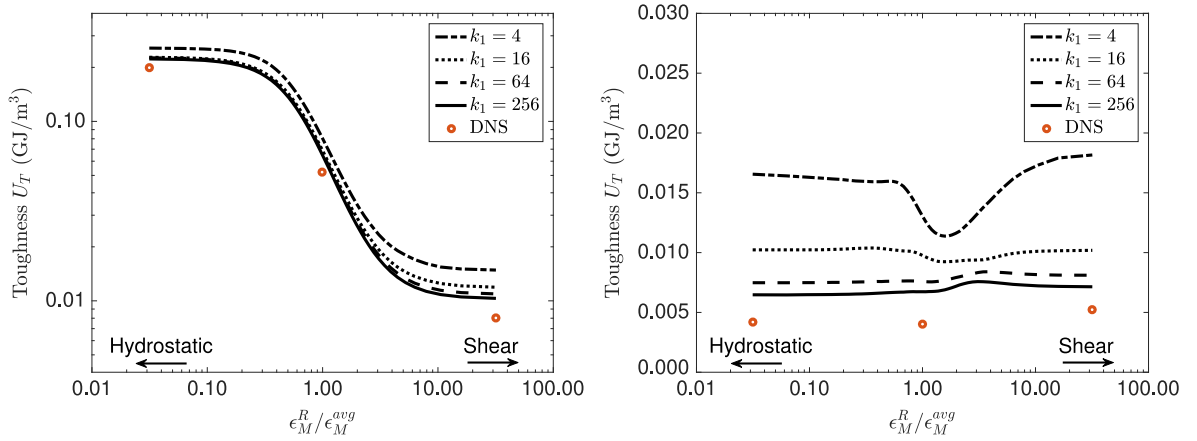


Fig. 10. The material toughness calculations for RVEs with hard inclusions (left) and soft inclusions (right).

The material toughness, U_T , is defined in Eq. (65). When computing the material toughness for each loading path, the loading direction, or the strain ratio $\epsilon_M^R / \epsilon_M^{avg}$, is fixed.

Fig. 10 shows the material toughness U_T of the RVE as a function of the ratio of ϵ_M^R to ϵ_M^{avg} . For hard inclusions, the toughness decreases monotonically with increasing strain ratio $\epsilon_M^R / \epsilon_M^{avg}$, and overall effective toughness is higher under the biaxial loading than by pure shearing loading by more than one order of magnitude. Similar to the matrix material, the effective damage evolution of the RVE with hard inclusions is dominated by the deviatoric component of the average stress, resulting in a low toughness under the pure shearing loading. The result for soft inclusions shows that the material toughness is no longer a monotonic function of the strain ratio, and that the material toughnesses does not vary much with the strain ratio. This can be explained by the fact that the soft inclusions undergo volumetric change under hydrostatic loading, which also induces high shear deformation and damage in the surrounding matrix material.

5.5. Energy regularization for calibrating damage parameters

The damage model should correctly reflect the energy dissipation in the macroscale fracture process. As a result, parameters in the damage evolution law need to be adjusted according to the measured fracture energy G_c under a given loading direction. Mathematically, the fracture energy should be

$$G_c = G_c^{DNS}(\alpha_0, \bar{\epsilon}^{cr}) = G_c^{SCA,k}(\alpha, \bar{\epsilon}^{cr}), \quad (67)$$

where k denotes the number of clusters in the SCA reduced-order model. The fracture energy G_c represents the dissipated energy due to fracture per unit crack surface in the macroscale, which serves as a physical material constant and should not depend on the choice of numerical models. The units of G_c is GJ/m². Given a length parameter l_h from the macroscale model, G_c can be expressed as

$$G_c = l_h U_F(\alpha, \bar{\epsilon}^{cr}), \quad (68)$$

where U_F represents the energy dissipated by fracture per unit volume at a material point. In the paper, the material toughness, U_T , is used to approximate the fracture energy, U_F ,

$$G_c \approx l_h U_T(\alpha, \bar{\epsilon}^{cr}), \quad (69)$$

The fracture energy, G_c , is usually measured experimentally, but for demonstration purposes, the DNS results are used as the reference solution for calibrating the damage evolution rate, α , and the critical plastic strain, $\bar{\epsilon}^{cr}$, in the SCA model for energy consistency. Since the length parameter, l_h , is determined by the macroscale model, one only needs to match the material toughness between the SCA and DNS RVE models:

$$U_T^{SCA,k}(\alpha, \bar{\epsilon}^{cr}) = U_T^{DNS}(\alpha_0, \bar{\epsilon}_0^{cr}). \quad (70)$$

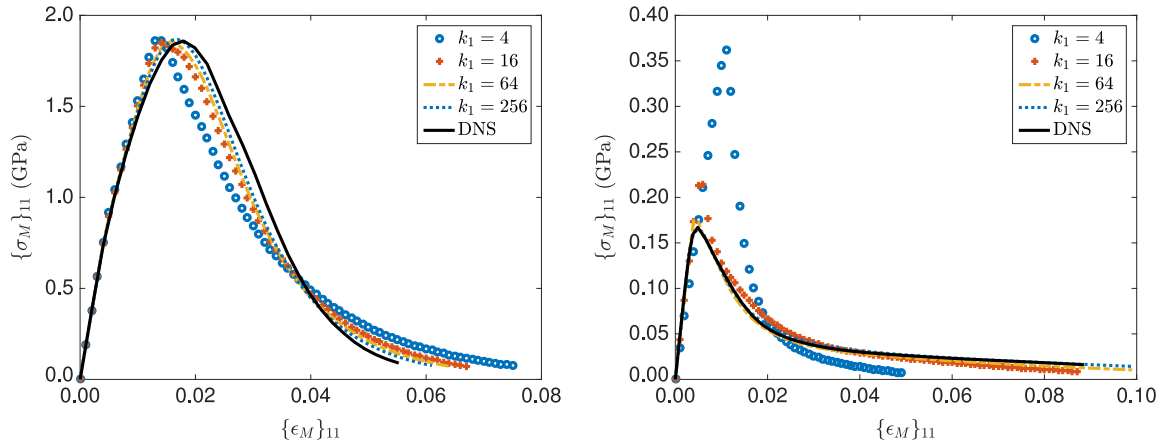


Fig. 11. The stress–strain curves of the damaged RVE with hard inclusions (left) and soft inclusions (right) for uniaxial tension loading. Damage parameters are calibrated using energy regularization.

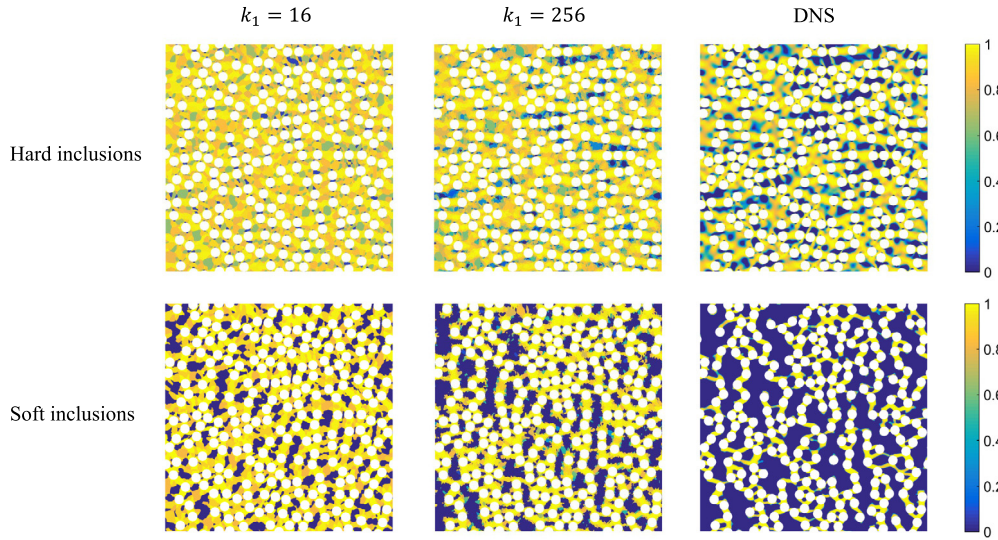


Fig. 12. RVE damage fields in the matrix phase at $\{\varepsilon_M\}_{11} = 0.04$ predicted by DNS and SCA following energy regularization for hard inclusions and soft inclusions. No damage is considered in the inclusion phase.

The damage parameters α_0 and $\bar{\varepsilon}_0^{\text{cr}}$ used for the DNS calculation are $\alpha_0 = 100$ and $\bar{\varepsilon}_0^{\text{cr}} = 0.02$. Additionally, it is important to match the maximum stress, σ_c , during the loading process, which corresponds to the ultimate strength of the material.

$$\sigma_c^{SCA,k}(\alpha, \bar{\varepsilon}^{\text{cr}}) = \sigma_c^{DNS}(\alpha_0, \bar{\varepsilon}_0^{\text{cr}}). \quad (71)$$

The damage parameters calibrated under uniaxial tension loading are provided in Table 4. The homogenized stress–strain curves following energy regularization are shown in Fig. 11. For the material with hard inclusions, it is possible to match the peak stress with very few clusters, but matching the damage evolution curve requires more clusters. For the material with soft inclusions, more clusters are required to match both the peak stress and the damage evolution curve. A comparison is provided in Fig. 12 between the damage fields from DNS and SCA following energy regularization. It can be seen that for both hard inclusions and soft inclusions, additional clusters improve the computation of the localized damage fields.

Table 4

Calibrated damage parameters (α , $\bar{\epsilon}^{\text{cr}}$) for SCA for different numbers of clusters using energy regularization. The damage parameters are unitless.

	Hard inclusions		Soft inclusions	
	α	$\bar{\epsilon}^{\text{cr}}$	α	$\bar{\epsilon}^{\text{cr}}$
$k_1 = 4$	52	0.0092	100	0.0015
$k_1 = 8$	62	0.0112	60	0.0015
$k_1 = 16$	63	0.0120	60	0.0020
$k_1 = 32$	67	0.0128	50	0.0020
$k_1 = 64$	72	0.0134	40	0.0020
$k_1 = 128$	77	0.0140	30	0.0020
$k_1 = 256$	81	0.0146	30	0.0025
DNS	100	0.02	100	0.02

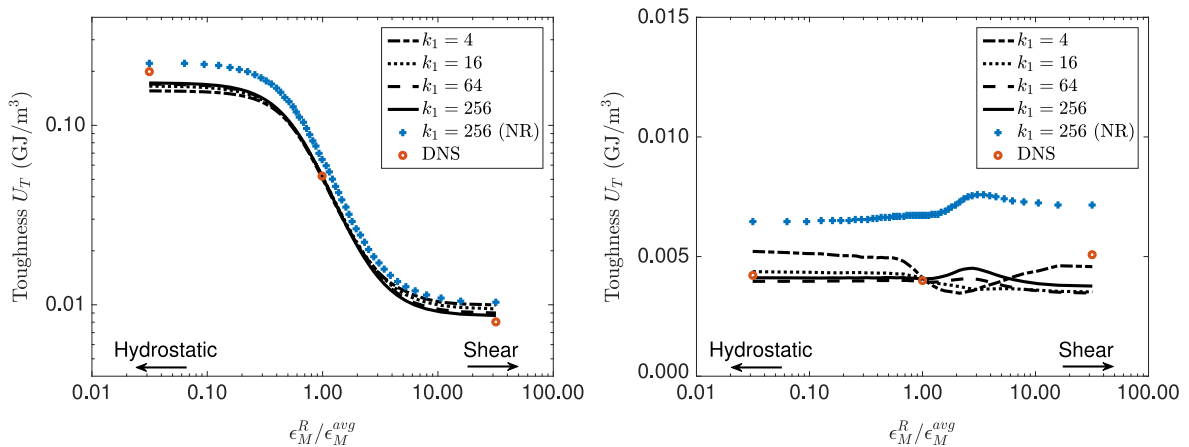


Fig. 13. The material toughness calculations following energy regularization for hard inclusions (left) and soft inclusions (right). The results without energy regularization are plotted for reference, and are denoted as (NR).

Fig. 13 shows good agreement between the toughness computed using SCA and DNS. In addition, the toughness results across the entire load spectrum agree much better after energy regularization, particularly for RVEs with soft inclusions. With only a small number of clusters, the SCA reduced order model with calibrated damage parameters can achieve good accuracy compared with DNS results.

6. Concurrent multiscale results and discussion

Concurrent multiscale simulations involving strain softening and localization are performed under two-dimensional plane strain conditions and in three dimensions. The proposed micro-damage homogenization scheme coupled with the SCA method is used. In these examples, the macroscale properties are determined by the microstructural morphologies and the microscale constituents. The SCA material database is compiled during the offline stage, greatly reducing the computational cost of analyzing the microscale RVE model with minimal loss of accuracy, and making the concurrent simulation computationally feasible. The homogenized material can predict the macroscale performance while capturing the physical phenomena appearing in the microscale.

6.1. 2D Double-notched plate

A 2D tensile specimen with rounded notches in two corners [54] is depicted in Fig. 14. The notches in the opposite corners cause a geometric stress concentration which will induce localization as the loaded upper edge of the specimen is displaced. The material properties used for the matrix and the inclusion material are given in Section 5.1; both hard and soft inclusions are analyzed. The simulations are conducted using the explicit finite element method and 2D plane

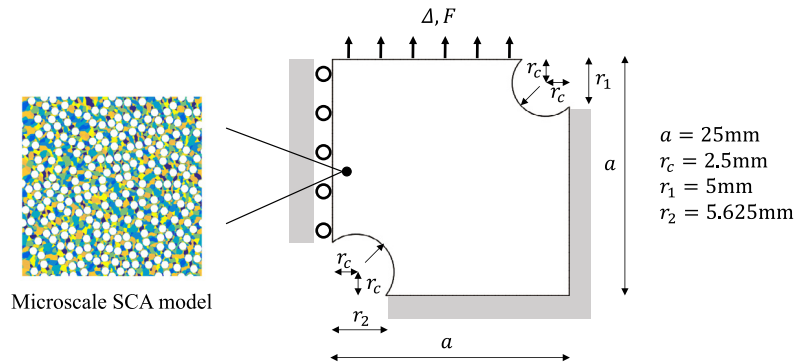


Fig. 14. Geometry of the double-notched specimen in the 2D plane-strain condition.

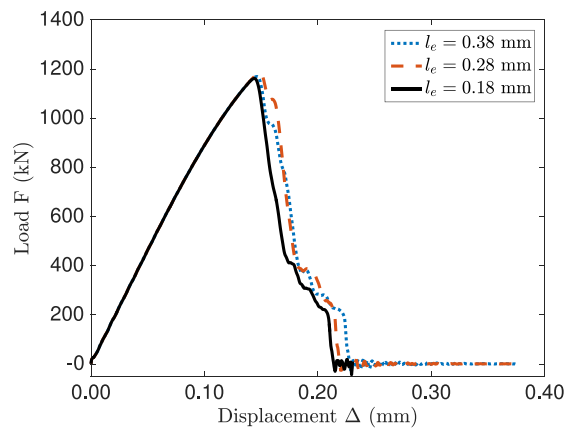


Fig. 15. Load-displacement curves with different mesh size l_e for hard inclusions. The non-local length parameter l_0 is 2 mm.

strain elements with reduced integration (one integration point per element), and the micro-damage algorithm with the SCA model is implemented as a user-defined material at each integration point. Specifically, LU decomposition in the Intel® Math Kernel Library (MKL) is utilized for solving the linear systems in the SCA model. A macroscopic element is deleted when the effective damage parameter d_M of its associated RVE reaches 0.99.

The effectiveness of the non-local formulation is first investigated without considering energy regularization. The microscale is modeled using an RVE with hard inclusions; the SCA database with 32 clusters in the matrix phase is used for the microstructural RVE calculation. Fig. 15 presents the load-displacement curves from the concurrent simulations for three different macroscale FE meshes shown in Fig. 16. A non-local length parameter of $l_0 = 2$ mm is used. Moreover, the crack patterns after the coupon failure for all three mesh sizes are also shown in Fig. 16. It can be concluded that given $l_0 > 4l_e$, the non-local formulation can effectively diminish the mesh-size dependency, as well as the pathological mesh dependency.

Fig. 17 shows the load-displacement curves for RVEs with hard inclusions and soft inclusions predicted using concurrent simulation without energy regularization. The numbers of clusters in phase 1 in the microscale reduced-order model ranges from 4 to 64. Since the concurrent simulation with microscale RVE modeled by DNS is computationally expensive, the multiscale DNS results are not provided for comparison. Faster convergence is observed in models with hard inclusions than those with soft inclusions. In addition, the predictions have a higher fidelity in the elasto-plastic regime than in the strain-softening regime. Increasing the number of clusters in the microscale RVE clearly improves the prediction, but the convergence rate is not satisfactory, similar to the convergence rates observed in Section 5.4.

Energy regularization is introduced to increase the fidelity of the calculation. The calibrated damage parameters for different numbers of clusters have been provided in Table 4. The load-displacement curves from the concurrent

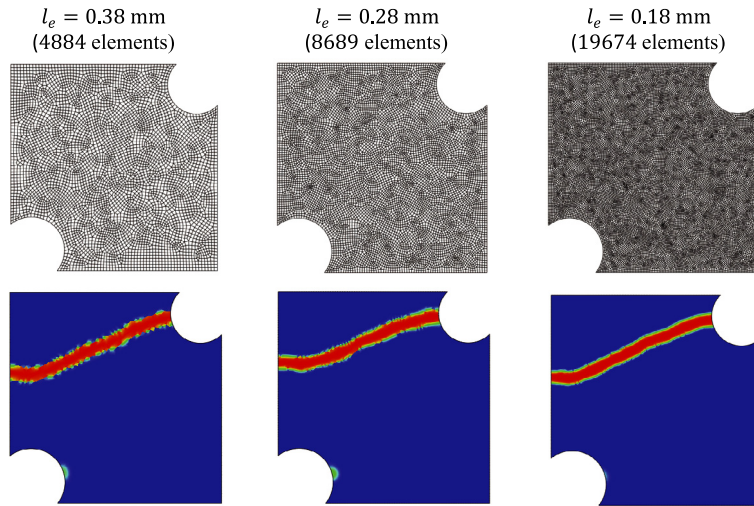


Fig. 16. Crack patterns with different mesh size l_e for hard inclusions. The non-local length parameter is $l_0 = 2$ mm. The SCA model has 32 clusters in the matrix phase ($k_1 = 32$).

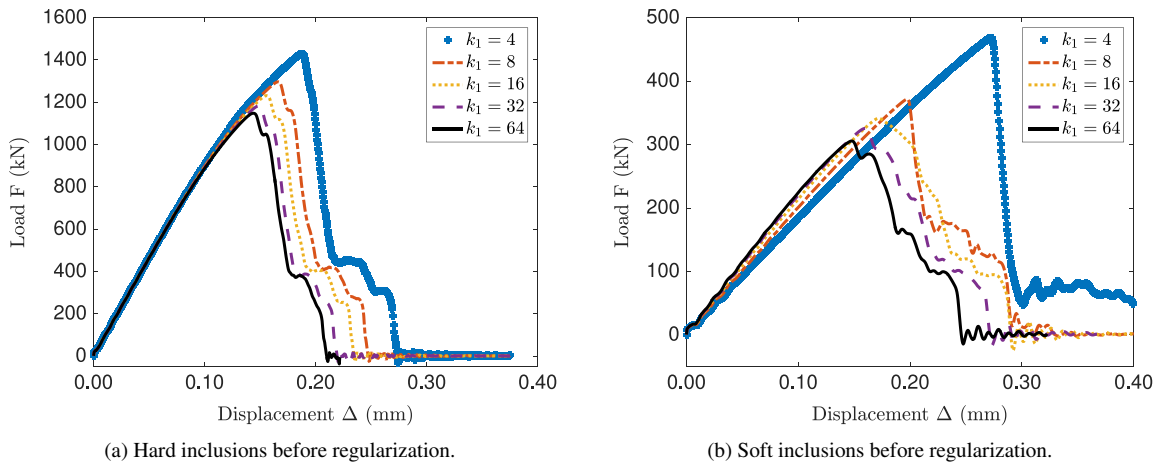


Fig. 17. Load–displacement curves predicted by SCA databases with different number clusters k_1 before energy regularization.

simulations after energy regularization are shown in Fig. 18. It can be seen that the accuracy and convergence rate with respect to the number of clusters have been improved for both hard and soft inclusions. Meanwhile, Fig. 19 presents the crack patterns from the concurrent simulation with energy regularization, which shows a consistent cracking pattern as the number of cluster is increased. Although the same microstructure and SCA database have been used, the crack patterns for hard and soft inclusions are noticeably different. The influence of micro-constituent on the macro-responses is captured by the concurrent simulation driven by the SCA database.

The computational times for the 2D concurrent simulations and k_1 ranging from 4 to 64 are listed in Table 5. The macroscale mesh size is $l_e = 0.28$ mm, and there are in total 8689 elements in the model. All the simulations are conducted on 24 cores (in a state-of-the art high performance computing cluster with the following compute nodes: Intel Haswell E5-2680v3 2.5 GHz 12-cores). A linear scalability with the number of cores is observed for small number of clusters. When $k_1 > 16$, the computational time of the concurrent simulation increases approximately as the square of k_1 . Based on the computational time of SCA ($k_1 = 4$) and DNS for the RVE calculation in Section 5, the estimated DNS time (FE^2) of the concurrent simulation would be 295 days (see Table 5).

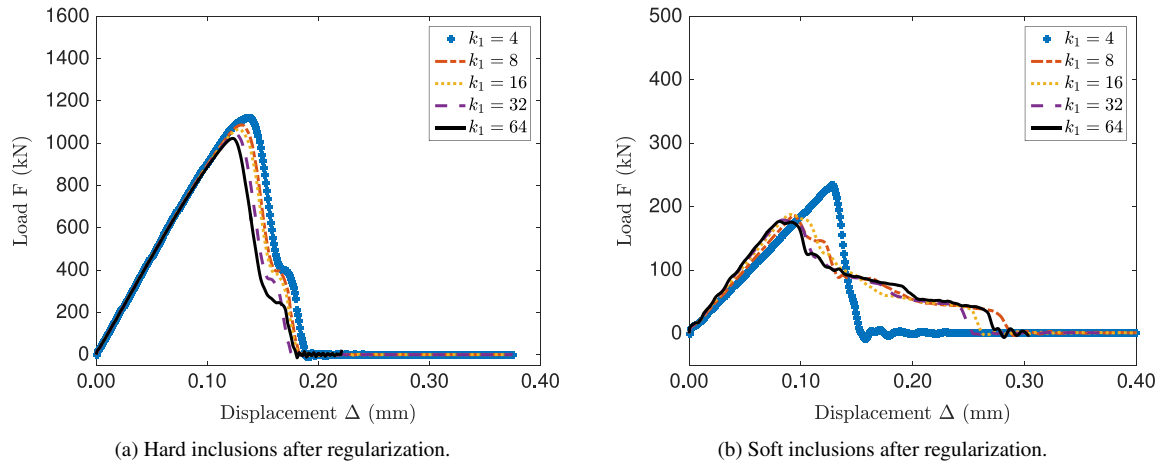


Fig. 18. Load–displacement curves predicted by SCA databases with different number clusters k_1 after energy regularization.

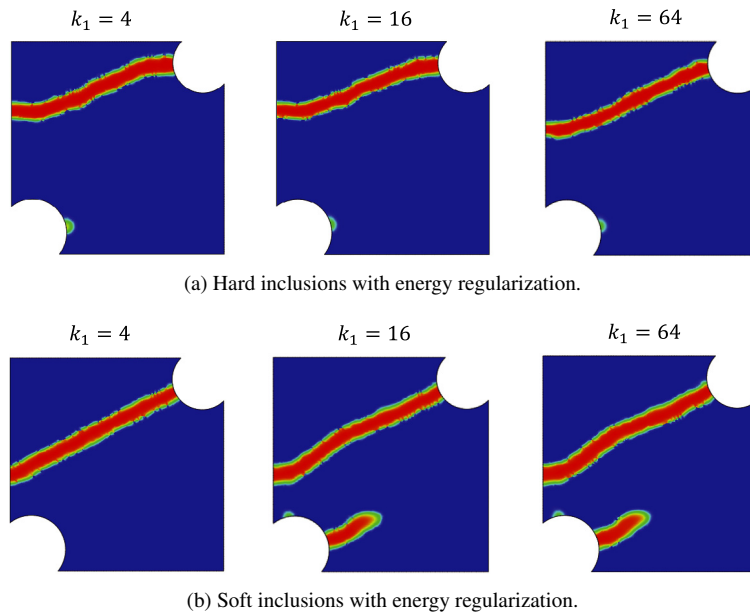


Fig. 19. Crack patterns predicted by SCA databases with different number clusters k_1 after energy regularization.

Table 5

Computational time of the 2D concurrent simulations of various numbers of clusters in phase 1 on 24 cores.

k_1	4	8	16	32	64	Estimated DNS time
Wall clock time (min)	19	44	117	416	1948	4.2×10^5 (295 days)
Speedup of SCA	2.2×10^4	9.5×10^3	3.6×10^3	1.0×10^3	216	NA

6.2. 3D Double-notched plate

The micro-damage algorithm and the SCA method are further applied to 3D concurrent simulations for the double-notched model shown in Fig. 20. The in-plane shape of the 3D model is identical to the 2D example shown in Fig. 14, and the applied boundary conditions are also identical to the 2D model. The thickness of the FE model is 8 mm. Symmetric boundary conditions are applied on the back face on the X-Y plane (no displacement in the Z-direction),

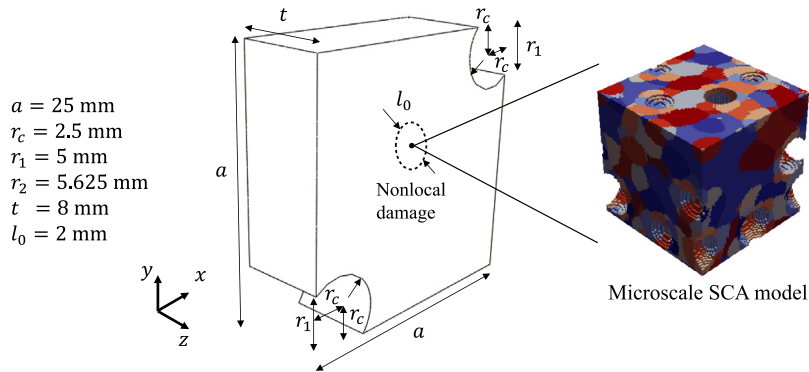


Fig. 20. Geometry of the 3D double-notched coupon and microscale SCA model with 8 clusters in the matrix phase. The non-local length parameter l_0 is equal to 2 mm.

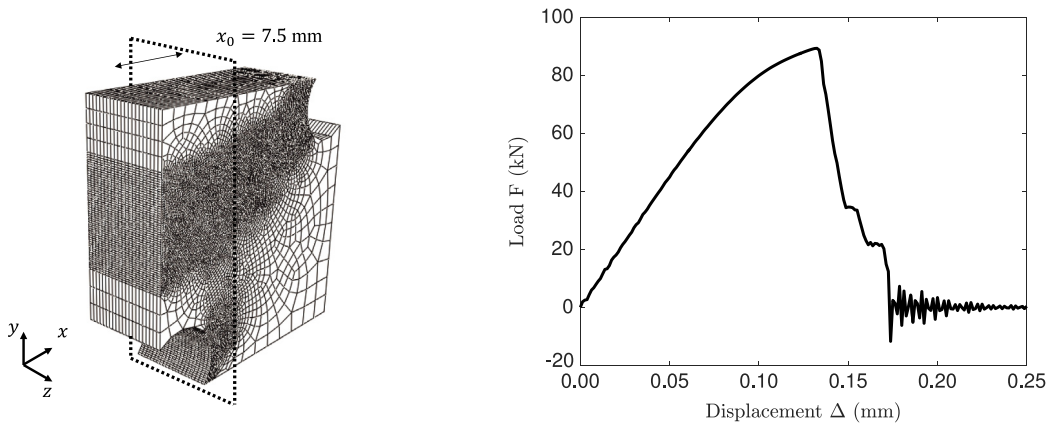


Fig. 21. Macroscale FE mesh with local refinement (left) and load-displacement curve of the 3D concurrent simulations with hard inclusions (right).

resulting in an effective total thickness of 16 mm. The non-local length parameter is $l_0 = 2 \text{ mm}$. The mesh is refined in the region containing the crack with the characteristic mesh size $l_e = 0.18 \text{ mm}$, so there are approximately 10 elements through the thickness of the damage region. For the macroscale FE model, there are in total 154,371 3D hex elements with reduced integration (one Gauss/integration point per element).

The microscale 3D RVE model has identical spherical inclusions embedded in the matrix, and the volume fraction of the inclusion phase is 20%. The corresponding DNS FE mesh for the RVE is $80 \times 80 \times 80$. In the microscale SCA model, there are 8 clusters in the matrix phase and 2 clusters in the inclusion phase. An RVE with hard inclusions is considered in the microscale. All the material parameters are the same as before (see Table 1). Specifically, the initial damage parameters $\alpha = 100$ and $\bar{\epsilon}^{cr} = 0.02$ are used. The macroscopic elements will be deleted when the effective damage parameter d_M of the RVE reaches 0.99.

The load-displacement curve from the concurrent simulations with hard inclusions is shown in Fig. 21, and the crack patterns at different loading states are also provided in Fig. 22. In addition, the microscale stress and damage fields are shown for RVEs at different integration points in the macroscale model. In the concurrent coupling, the microscale RVE reduced order model not only provides the overall stress-strain responses for the macroscale FE model, but also stores local quantities such as plastic strain and damage parameter inside the microstructure/clusters. It can be observed that the concurrent simulations are able to demonstrate a non-planar crack through the cross-section due to the constraint effects of the thick coupon. In addition, the crack front is curved, as one can see from the snapshots at displacement $\Delta = 0.15 \text{ mm}$. The damaged region initiates at the center of the model cross-section and propagates forward and toward the boundaries.

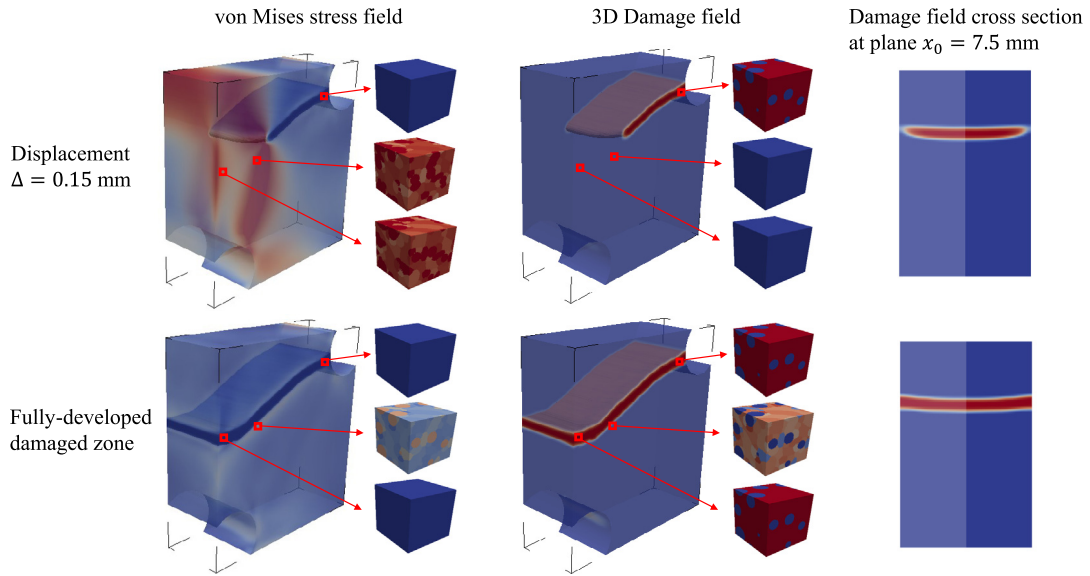


Fig. 22. The von Mises stress distributions and crack patterns of the 3D concurrent simulations at two loading states. The microscale stress and damage fields inside the RVE are shown in sequence at three different integration points marked in the macroscale model.

Table 6

Computational time of the 3D concurrent simulations of various numbers of clusters in phase 1 on 72 cores.

	SCA($k_1 = 8$)	Estimated DNS time
Wall clock time (min)	56 h	1.1×10^5 days
Speedup of SCA	4.6×10^4	NA

Due to the limitation of computational resources, convergence tests and energy regularization have not yet been performed for the 3D problem, but these preliminary concurrent simulations demonstrate the capability of the SCA multiscale modeling framework for capturing the microstructural effect. By using 72 cores (Intel Haswell E5-2680v3 2.5 GHz 12-cores), the concurrent simulation with the Intel MKL library required approximately 56 h. Based on the time comparison for the 3D RVE computation [1], the estimated DNS time for the same concurrent simulation, with the original $80 \times 80 \times 80$ FEM mesh in the microscale and the same computational resources, would be more than 1.1×10^5 days (see Table 6).

7. Conclusion

In this paper, a stable micro-damage algorithm has been introduced which removes the need for a material length parameter in the microstructural RVE. By matching the effective elastic strains of the undamaged and damaged RVE, strain localization is avoided in the microscale RVE, and the homogenized behavior in the strain-softening regime is independent of the RVE size. No material length parameter is required in the microscale, and the RVE homogenization is able to capture the driving mechanisms of the damage process.

A macroscopic material length parameter is utilized to alleviate the material instability associated with strain softening behavior in the macroscopic calculation. It is demonstrated that the non-local damage model with the length parameter can effectively remove the pathological mesh dependence.

Self-consistent clustering analysis (SCA) provides an efficient computational technique for an RVE undergoing nonlinear history-dependent deformation. A good tradeoff between efficiency and accuracy is possible with SCA through the domain decomposition based on k-means clustering of high-fidelity data and the micromechanics-based self-consistent scheme. A new projection-based self-consistent scheme for solving the Lippmann–Schwinger equation is proposed in the SCA online/prediction stage, which is able to handle the RVE problem under complex loadings in

Table 7

Summary of the computational time for the RVE homogenization and concurrent simulations. k denotes the total number of clusters in the SCA database.

	2D RVE		2D concurrent		3D concurrent	
	SCA ($k = 1536$)	DNS	SCA ($k = 96$)	DNS (est.)	SCA ($k = 10$)	DNS (est.)
Time	118 s	7814 s	1948 min	4.2×10^5 min	56 h	2.4×10^5 h
Speedup	66	NA	216	NA	4.6×10^4	NA

a concurrent simulation. With the same SCA database, different macroscale crack paths are predicted for RVEs with different inclusion properties (hard inclusions versus soft inclusions). The proposed method is general and can be applied to various material systems with more complex settings.

A solution comparison with DNS has shown that the proposed micro-damage methodology coupled with SCA is capable of achieving accurate solutions at an incredible reduction of computational expense (see Table 7). For a 2D plane strain problem, the solution time using SCA is 1948 min using 64 clusters compared with an estimated 295 days required for a DNS calculation. For a 3D problem, the SCA solution time is 56 h, compared with an estimated 1.1×10^5 days using DNS.

Acknowledgments

Z.L. and W.K.L. warmly thank the support from AFOSR Grant No. FA9550-14-1-0032 and National Institute of Standards and Technology and Center for Hierarchical Materials Design (CHiMaD) under Grant Nos. 70NANB13HI94 and 70NANB14H012.

Appendix A. Clustering of the strain concentration tensor

Details of clustering the material points in the RVE are discussed in this Appendix. For a 2-dimensional model, the strain concentration tensor $\mathbf{A}(\mathbf{x})$ in each material point has 9 independent components. The format of the raw data for a 2D material is shown below

DataIndex	A_{11}	A_{22}	A_{33}	A_{12}	A_{21}	A_{23}	A_{32}	A_{13}	A_{31}
1	–	–	–	–	–	–	–	–	–
2	–	–	–	–	–	–	–	–	–
\vdots			\vdots			\vdots			\vdots
N	–	–	–	–	–	–	–	–	–

where N is the total number of discretization points in the DNS. For the 1200×1200 mesh used in the paper, N is equal to 1 440 000. For a 3-dimensional model, $\mathbf{A}(\mathbf{x})$ has 36 independent components.

The next step is to perform the domain decomposition by grouping similar data points using k-means clustering [52]. Mathematically, given a set of strain concentration tensors, the objective of k-means clustering is to minimize the within-cluster least squares sum for the k sets $\mathbf{S} = \{S^1, S^2, \dots, S^k\}$ to obtain the shape of the clusters:

$$\mathbf{S} = \operatorname{argmin}_{\mathbf{S}'} \sum_{J=1}^k \sum_{n \in S^J} \|\mathbf{A}_n - \bar{\mathbf{A}}_J\|^2, \quad (\text{A.1})$$

where \mathbf{A}_n is the strain concentration tensor of the n th data point, and $\bar{\mathbf{A}}_J$ is the mean of all the strain concentration tensors at the points within the cluster S_J . The above norm is defined as usual, e.g. for a general second-order matrix \mathbf{Z} of dimension $m \times m$

$$\|\mathbf{Z}\| = \sqrt{\sum_{i=1}^m \sum_{j=1}^m z_{ij}^2} = \sqrt{\operatorname{trace}(\mathbf{Z}^T \mathbf{Z})}, \quad (\text{A.2})$$

and is called the Frobenius norm of matrix \mathbf{Z} . In this paper, the standard algorithm (Lloyd's algorithm) [55] is used to solve the k-means clustering problem, which is essentially an optimization process minimizing the sum in Eq. (A.1).

At the initialization step, k data points are randomly selected from the data set and served as the initial means (Forgy method [56]). The algorithm then iterates between the following two steps,

1. Assignment step: Each data point is assigned to the cluster whose mean is nearest to the data point. In other words, within the t th iteration, $\forall \{\mathbf{A}_n\} \in S_I^{(t)}$

$$\|\{\mathbf{A}_n\} - \bar{\mathbf{A}}_I^{(t)}\|^2 \leq \|\{\mathbf{A}_n\} - \bar{\mathbf{A}}_J^{(t)}\|^2 \quad \forall J, J \neq I. \quad (\text{A.3})$$

2. Update step: The mean values of the data points in the new cluster are recalculated for iteration $t + 1$,

$$\bar{\mathbf{A}}_I^{(t)} = \frac{1}{N_I^{(t)}} \sum_{\{\mathbf{A}_n\} \in S_I^{(t)}} \{\mathbf{A}_n\}, \quad (\text{A.4})$$

where $N_I^{(t)}$ is the number of data points in cluster $S_I^{(t)}$.

When the assignment of data points no longer changes, the algorithm is said to converge to a local optimum. Finally, it should be noted that other clustering methods can also be applied for this problem, such as the density-based spatial clustering of applications with noise (DBSCAN) method [57].

Appendix B. Computing the interaction tensor

In the discretized/reduced Lippmann–Schwinger equation, the piecewise uniform assumption can be utilized to extract the interaction tensor \mathbf{D}^{IJ} , which represents the influence of the stress in the J th cluster on the strain in the I th cluster [1]. In a periodic RVE domain Ω , the interaction tensor can be written as a convolution of the Green's function and the characteristic functions,

$$\mathbf{D}^{IJ} = \frac{1}{c^I |\Omega|} \int_{\Omega} \int_{\Omega} \chi^I(\mathbf{x}) \chi^J(\mathbf{x}') \Phi^0(\mathbf{x}, \mathbf{x}') d\mathbf{x}' d\mathbf{x}, \quad (\text{B.1})$$

where c^I is the volume fraction of the I th cluster and $|\Omega|$ is the volume of the RVE domain. $\Phi^0(\mathbf{x}, \mathbf{x}')$ is the fourth-order periodic Green's function associated with an isotropic linear elastic reference material and its stiffness tensor is \mathbf{C}^0 . As will be shown in Section 4.2, this reference material is introduced in the online stage as a homogeneous media to formulate the Lippmann–Schwinger integral equation. With the periodicity of the RVE, $\Phi^0(\mathbf{x}, \mathbf{x}')$ takes a simple form for isotropic materials in the Fourier space,

$$\hat{\Phi}^0(\boldsymbol{\xi}) = \frac{1}{4\mu^0} \hat{\Phi}^1(\boldsymbol{\xi}) + \frac{\lambda^0 + \mu^0}{\mu^0(\lambda^0 + 2\mu^0)} \hat{\Phi}^2(\boldsymbol{\xi}), \quad (\text{B.2})$$

with

$$\hat{\Phi}_{ijkl}^1(\boldsymbol{\xi}) = \frac{1}{|\boldsymbol{\xi}|^2} (\delta_{ik} \xi_j \xi_l + \delta_{il} \xi_j \xi_k + \delta_{jl} \xi_i \xi_k + \delta_{jk} \xi_i \xi_l) \quad (\text{B.3})$$

$$\hat{\Phi}_{ijkl}^2(\boldsymbol{\xi}) = -\frac{\xi_i \xi_j \xi_k \xi_l}{|\boldsymbol{\xi}|^4}, \quad (\text{B.4})$$

where $\boldsymbol{\xi}$ is the coordinate in Fourier space corresponding to \mathbf{x} in real space, and δ_{ij} is the Kronecker delta function. λ^0 and μ^0 are Lamé constants of the reference material. The expression of $\hat{\Phi}_{ijkl}^0(\boldsymbol{\xi})$ is not well defined at frequency point $\boldsymbol{\xi} = \mathbf{0}$. However, imposing by the boundary conditions for deriving the Green's function, a uniformly distributed polarization stress field will not induce any strain field inside the RVE, which indicates

$$\hat{\Phi}_{ijkl}^0(\boldsymbol{\xi} = \mathbf{0}) = \mathbf{0}. \quad (\text{B.5})$$

Based on Eq. (B.2), the convolution term in the spatial domain in Eq. (B.1) can be translated into a direct multiplication at each point $\boldsymbol{\xi}$ in the frequency domain using a Fourier transformation,

$$\bar{\Phi}_J^0(\mathbf{x}) = \int_{\Omega} \chi^J(\mathbf{x}') \Phi^0(\mathbf{x}, \mathbf{x}') d\mathbf{x}' = \mathcal{F}^{-1} \left(\hat{\chi}^J(\boldsymbol{\xi}) \hat{\Phi}^0(\boldsymbol{\xi}) \right). \quad (\text{B.6})$$

It can be seen from Eq. (B.3) and (B.4) that $\hat{\Phi}^1(\boldsymbol{\xi})$ and $\hat{\Phi}^2(\boldsymbol{\xi})$ are independent of the material properties, meaning that they can be computed one time only in the offline stage. If the reference material is changed in the self-consistent scheme at the online stage, only the coefficients relating to its Lamé constants in Eq. (B.2) need to be updated.

Appendix C. Newton's iteration in the online stage

In the implicit scheme, the residual $\{\mathbf{r}\} = \{\mathbf{r}^1; \dots; \mathbf{r}^k; \mathbf{r}^{k+1}\}$ is linearized with respect to $\{\Delta\boldsymbol{\epsilon}\}$. Dropping terms of higher order than linear gives

$$\{\mathbf{r}\} + \{\mathbf{M}\}\{\Delta\boldsymbol{\epsilon}\} = \mathbf{0} \quad \text{with } \{\mathbf{M}\} = \frac{\partial\{\mathbf{r}\}}{\partial\{\Delta\boldsymbol{\epsilon}\}}, \quad (\text{C.1})$$

where $\{\mathbf{M}\}$ is called the system Jacobian matrix. For $I, J = 1, 2, \dots, k$,

$$\mathbf{M}^{IJ} = \delta_{IJ}\mathbf{I} + \mathbf{D}^{IJ} : (\mathbf{C}_{alg}^J - \mathbf{C}^0) \quad \text{and} \quad \mathbf{M}^{I(k+1)} = -\mathbf{I}, \quad (\text{C.2})$$

where δ_{IJ} is the Kronecker delta in terms of indices I and J , and \mathbf{I} is the fourth-order identity tensor. \mathbf{C}_{alg}^J is the so-called algorithmic stiffness tensor of the material in the J th cluster and is an output of the local constitutive law for the current strain increment in that cluster $\Delta\boldsymbol{\epsilon}_n^J$,

$$\mathbf{C}_{alg}^J = \frac{\partial\Delta\boldsymbol{\sigma}^J}{\partial\Delta\boldsymbol{\epsilon}^J}. \quad (\text{C.3})$$

Although local material damage is decoupled with the equilibrium condition to avoid material instability in this paper, it is still possible to introduce the damage into the local constitutive law and \mathbf{C}_{alg}^J can be written as

$$\mathbf{C}_{alg}^J = (1 - d^J) \frac{\partial\Delta\boldsymbol{\sigma}_{ud}^J}{\partial\Delta\boldsymbol{\epsilon}^J}, \quad (\text{C.4})$$

where $\partial\Delta\boldsymbol{\sigma}_{ud}^J/\partial\Delta\boldsymbol{\epsilon}^J$ represents the algorithmic stiffness tensor of the undamaged pure elasto-plastic material. Under the macro-strain constraint, the remaining components in the system Jacobian matrix are

$$\mathbf{M}^{(k+1)I} = c^I\mathbf{I} \quad \text{and} \quad \mathbf{M}^{(k+1)(k+1)} = \mathbf{0}. \quad (\text{C.5})$$

For macro-stress constraint,

$$\mathbf{M}^{(k+1)I} = c^I\mathbf{C}_{alg}^I \quad \text{and} \quad \mathbf{M}^{(k+1)(k+1)} = \mathbf{0}. \quad (\text{C.6})$$

Finally, the correction of the incremental strain can be expressed as

$$\{\Delta\boldsymbol{\epsilon}\} = -\{\mathbf{M}\}^{-1}\{\mathbf{r}\}. \quad (\text{C.7})$$

Based on the updated incremental strain, the constitutive relationship in each cluster can then be used to compute the new incremental stress $\{\Delta\boldsymbol{\sigma}\} = \{\Delta\boldsymbol{\sigma}^1; \dots; \Delta\boldsymbol{\sigma}^k\}$. If $\Delta\boldsymbol{\sigma}^I$ and $\Delta\boldsymbol{\epsilon}^I$ have a nonlinear relation, several iterations are needed so that the residual $\{\mathbf{r}\}$ can vanish.

References

- [1] Z. Liu, M.A. Bessa, W.K. Liu, Self-consistent clustering analysis: An efficient multi-scale scheme for inelastic heterogeneous materials, *Comput. Methods Appl. Mech. Engrg.* 306 (2016) 319–341.
- [2] C. McVeigh, W.K. Liu, Linking microstructure and properties through a predictive multiresolution continuum, *Comput. Methods Appl. Mech. Engrg.* 197 (41) (2008) 3268–3290.
- [3] C. McVeigh, F. Vernerey, W.K. Liu, L.C. Brinson, Multiresolution analysis for material design, *Comput. Methods Appl. Mech. Engrg.* 195 (37) (2006) 5053–5076.
- [4] M.G. Geers, V.G. Kouznetsova, W. Brekelmans, Multi-scale computational homogenization: Trends and challenges, *J. Comput. Appl. Math.* 234 (7) (2010) 2175–2182.
- [5] Z.P. Bažant, Can multiscale-multiphysics methods predict softening damage and structural failure?, *Int. J. Multiscale Comput. Eng.* 8 (1) (2010).
- [6] A.L. Gurson, Continuum theory of ductile rupture by void nucleation and growth: Part I—Yield criteria and flow rules for porous ductile media, *J. Eng. Mater. Technol.* 99 (1) (1977) 2–15.
- [7] Z.P. Bažant, M. Jirásek, Nonlocal integral formulations of plasticity and damage: survey of progress, *J. Eng. Mech.* 128 (11) (2002) 1119–1149.
- [8] F. Vernerey, W.K. Liu, B. Moran, Multi-scale micromorphic theory for hierarchical materials, *J. Mech. Phys. Solids* 55 (12) (2007) 2603–2651.
- [9] F. Vernerey, W.K. Liu, B. Moran, G. Olson, A micromorphic model for the multiple scale failure of heterogeneous materials, *J. Mech. Phys. Solids* 56 (4) (2008) 1320–1347.
- [10] S. Forest, Micromorphic approach for gradient elasticity, viscoplasticity, and damage, *J. Eng. Mech.* 135 (3) (2009) 117–131.
- [11] C. Miehe, F. Welschinger, M. Hofacker, Thermodynamically consistent phase-field models of fracture: Variational principles and multi-field FE implementations, *Internat. J. Numer. Methods Engrg.* 83 (10) (2010) 1273–1311.

- [12] C. Miehe, M. Hofacker, L.-M. Schaezel, F. Aldakheel, Phase field modeling of fracture in multi-physics problems. Part II. Coupled brittle-to-ductile failure criteria and crack propagation in thermo-elastic-plastic solids, *Comput. Methods Appl. Mech. Engrg.* 294 (2015) 486–522.
- [13] Z.P. Bažant, B.H. Oh, Crack band theory for fracture of concrete, *Mat. Constr.* 16 (3) (1983) 155–177.
- [14] A. Pandolfi, M. Ortiz, An eigeneration approach to brittle fracture, *Internat. J. Numer. Methods Engrg.* 92 (8) (2012) 694–714.
- [15] J.P. Holdren, et al., Materials Genome Initiative: Strategic Plan, Vol. 6, Office of Science and Technology Policy, Washington DC, 2014.
- [16] W.K. Liu, L. Siad, R. Tian, S. Lee, D. Lee, X. Yin, W. Chen, S. Chan, G.B. Olson, L.-E. Lindgen, et al., Complexity science of multiscale materials via stochastic computations, *Internat. J. Numer. Methods Engrg.* 80 (6–7) (2009) 932–978.
- [17] E.A. de Souza Neto, D. Peric, D. Owen, *Computational Methods for Plasticity: Theory and Applications*, Wiley, 2008.
- [18] L. Xue, T. Wierzbicki, Ductile fracture initiation and propagation modeling using damage plasticity theory, *Eng. Fract. Mech.* 75 (11) (2008) 3276–3293.
- [19] L. Xue, Constitutive modeling of void shearing effect in ductile fracture of porous materials, *Eng. Fract. Mech.* 75 (11) (2008) 3343–3366.
- [20] P. Camanho, M. Bessa, G. Catalanotti, M. Vogler, R. Rolfes, Modeling the inelastic deformation and fracture of polymer composites –Part II: Smeared crack model, *Mech. Mater.* 59 (0) (2013) 36–49.
- [21] F. Feyel, J.-L. Chaboche, FE^2 multiscale approach for modelling the elastoviscoplastic behaviour of long fibre SiC/Ti composite materials, *Comput. Methods Appl. Mech. Engrg.* 183 (3) (2000) 309–330.
- [22] V. Kouznetsova, M.G.D. Geers, W.A.M. Brekelmans, Multi-scale constitutive modelling of heterogeneous materials with a gradient-enhanced computational homogenization scheme, *Internat. J. Numer. Methods Engrg.* 54 (8) (2002) 1235–1260.
- [23] F. Feyel, A multilevel finite element method (FE^2) to describe the response of highly non-linear structures using generalized continua, *Comput. Methods Appl. Mech. Engrg.* 192 (28–30) (2003) 3233–3244.
- [24] G.J. Wagner, W.K. Liu, Coupling of atomistic and continuum simulations using a bridging scale decomposition, *J. Comput. Phys.* 190 (1) (2003) 249–274.
- [25] H. Kadowaki, W.K. Liu, Bridging multi-scale method for localization problems, *Comput. Methods Appl. Mech. Engrg.* 193 (30–32) (2004) 3267–3302.
- [26] H. Kadowaki, W.K. Liu, A multiscale approach for the micropolar continuum model, *Comput. Model. Eng. Sci.* 7 (3) (2005) 269–282.
- [27] H.S. Park, E.G. Karpov, P.A. Klein, W.K. Liu, Three-dimensional bridging scale analysis of dynamic fracture, *J. Comput. Phys.* 207 (2) (2005) 588–609.
- [28] S. Tang, T.Y. Hou, W.K. Liu, A pseudo-spectral multiscale method: Interfacial conditions and coarse grid equations, *J. Comput. Phys.* 213 (1) (2006) 57–85.
- [29] M. Bessa, R. Bostanabad, Z. Liu, A. Hu, D. Apley, C. Brinson, W. Chen, W.K. Liu, A framework for data-driven analysis of materials under uncertainty: Countering the curse of dimensionality, *Comput. Methods Appl. Mech. Engrg.* 320 (2017) 633–667.
- [30] J.D. Eshelby, The determination of the elastic field of an ellipsoidal inclusion, and related problems, *Proc. Roy. Soc. Lond. A* 241 (1226) (1957) 376–396. The Royal Society.
- [31] Z. Hashin, S. Shtrikman, A variational approach to the theory of the elastic behaviour of multiphase materials, *J. Mech. Phys. Solids* 11 (2) (1963) 127–140.
- [32] R. Hill, A self-consistent mechanics of composite materials, *J. Mech. Phys. Solids* 13 (4) (1965) 213–222.
- [33] Z. Liu, J.A. Moore, S.M. Aldousari, H.S. Hedia, S.A. Asiri, W.K. Liu, A statistical descriptor based volume-integral micromechanics model of heterogeneous material with arbitrary inclusion shape, *Comput. Mech.* (2015) 1–19.
- [34] Z. Liu, J.A. Moore, W.K. Liu, An extended micromechanics method for probing interphase properties in polymer nanocomposites, *J. Mech. Phys. Solids* 95 (2016) 663–680.
- [35] T. Belytschko, S. Loehnert, J.-H. Song, Multiscale aggregating discontinuities: A method for circumventing loss of material stability, *Internat. J. Numer. Methods Engrg.* 73 (6) (2008) 869–894.
- [36] H. Moulinec, P. Suquet, A numerical method for computing the overall response of nonlinear composites with complex microstructure, *Comput. Methods Appl. Mech. Engrg.* 157 (1–2) (1998) 69–94.
- [37] B. Le, J. Yvonnet, Q.-C. He, Computational homogenization of nonlinear elastic materials using neural networks, *Internat. J. Numer. Methods Engrg.* 104 (12) (2015) 1061–1084.
- [38] J. Yvonnet, E. Monteiro, Q.-C. He, Computational homogenization method and reduced database model for hyperelastic heterogeneous structures, *Int. J. Multiscale Comput. Eng.* 11 (3) (2013).
- [39] R. Ibañez, D. Borzacchiello, J.V. Aguado, E. Abisset-Chavanne, E. Cueto, P. Ladeveze, F. Chinesta, Data-driven non-linear elasticity: constitutive manifold construction and problem discretization, *Comput. Mech.* (2017) 1–14.
- [40] J. Michel, P. Suquet, Nonuniform transformation field analysis, *Int. J. Solids Struct.* 40 (25) (2003) 6937–6955.
- [41] J. Chaboche, P. Kanouté, A. Roos, On the capabilities of mean-field approaches for the description of plasticity in metal matrix composites, *Int. J. Plast.* 21 (7) (2005) 1409–1434.
- [42] J.-C. Michel, P. Suquet, A model-reduction approach in micromechanics of materials preserving the variational structure of constitutive relations, *J. Mech. Phys. Solids* 90 (2016) 254–285.
- [43] K. Karhunen, *Zur spektraltheorie stochastischer prozesse*, Suomalainen tiedeakatemia, 1946.
- [44] M. Loève, *Probability Theory; Foundations, Random Sequences*, D. Van Nostrand Company, New York, 1955.
- [45] I. Jolliffe, *Principal component analysis*, Wiley Online Library, 2002.
- [46] J. Yvonnet, Q.-C. He, The reduced model multiscale method (r3m) for the non-linear homogenization of hyperelastic media at finite strains, *J. Comput. Phys.* 223 (1) (2007) 341–368.
- [47] P. Kerfriden, O. Gouri, T. Rabczuk, S.P.-A. Bordas, A partitioned model order reduction approach to rationalise computational expenses in nonlinear fracture mechanics, *Comput. Methods Appl. Mech. Engrg.* 256 (2013) 169–188.

- [48] J. Oliver, M. Caicedo, A. Huespe, J. Hernández, E. Roubin, Reduced order modeling strategies for computational multiscale fracture, *Comput. Methods Appl. Mech. Engrg.* 313 (2017) 560–595.
- [49] C. Tasan, J. Hoefnagels, M. Geers, Identification of the continuum damage parameter: An experimental challenge in modeling damage evolution, *Acta Mater.* 60 (8) (2012) 3581–3589.
- [50] W.K. Liu, Y. Chen, Wavelet and multiple scale reproducing kernel methods, *Internat. J. Numer. Methods Fluids* 21 (10) (1995) 901–931.
- [51] S. Li, W.K. Liu, Moving Least Square Reproducing Kernel Method (III): Wavelet Packet & its Applications, *Methods* 7825 (96) (1996) 1–52.
- [52] J. MacQueen, Some methods for classification and analysis of multivariate observations, in: *Proceedings of the Fifth Berkeley Symposium on Mathematical Statistics and Probability*, Oakland, CA, USA, Vol. 1, no. 14, 1967, pp. 281–297.
- [53] I.H. Witten, E. Frank, *Data Mining: Practical Machine Learning Tools and Techniques*, Morgan Kaufmann, 2005.
- [54] J. Mediavilla Varas, *Continuous and discontinuous modelling of ductile fracture* (Ph.D. Thesis), Eindhoven University of Technology, 2005.
- [55] S.P. Lloyd, Least squares quantization in PCM, *IEEE Trans. Inf. Theory* 28 (2) (1982) 129–137.
- [56] E.W. Forgy, Cluster analysis of multivariate data: efficiency versus interpretability of classifications, *Biometrics* 21 (1965) 768–769.
- [57] M. Ester, H.-P. Kriegel, J. Sander, X. Xu, A density-based algorithm for discovering clusters in large spatial databases with noise, *Kdd* 96 (34) (1996) 226–231.